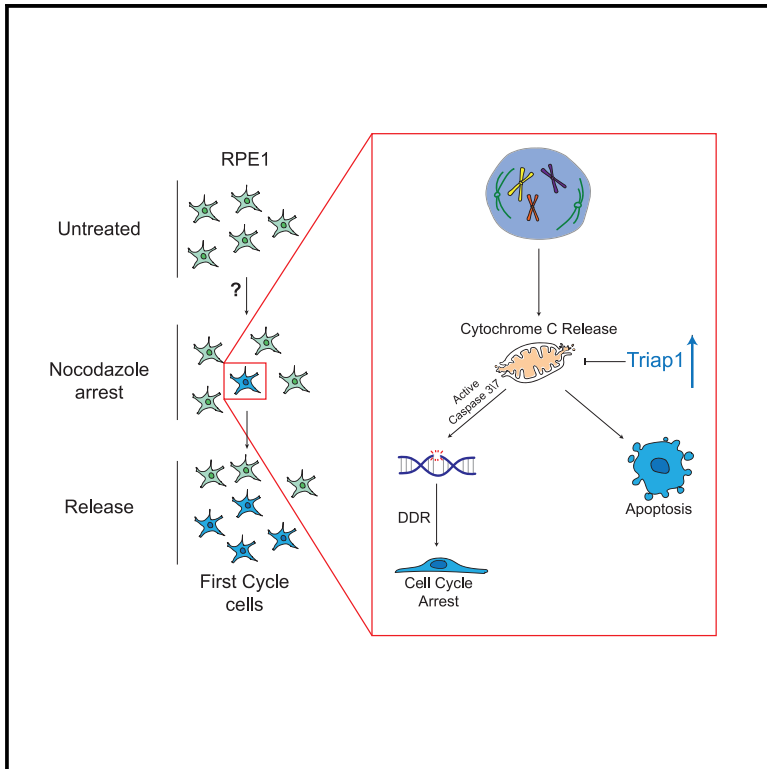# Cell Reports

Triap1 upregulation promotes escape from mitotic-slippage-induced G1 arrest

Graphical abstract

Authors

Mattia Pavani, Elena Chiroli,
Camilla Cancrini, ..., Luca L. Fava,
Tiziana Lischetti, Andrea Ciliberto

Correspondence

mattia.pavani@ifom.eu (M.P.),
tiziana.lischetti@icloud.com (T.L.),
andrea.ciliberto@ifom.eu (A.C.)

In brief

Antimitotic drugs impair microtubule dynamics and cause cells to arrest in mitosis or die due to DNA damage. Pavani et al. show that a fraction of cells escapes the arrest and restores proliferation and, when treated a second time, can repress cell death and decrease the extent of DNA damage.

Highlights

- Cells arrested by nocodazole accumulate DNA damage but recover growth after G1 arrest

- When treated for a second time, cells accumulate less DNA damage and recover faster

- The expression of about 100 proteins, including Triap1, is altered

- Increased Triap1 expression decreases DNA damage and accounts for the faster recovery

CellPress

Article

Triap1 upregulation promotes escape from mitotic-slippage-induced G1 arrest

Mattia Pavani,[1,*] Elena Chiroli,[1] Camilla Cancrini,[1] Fridolin Gross,[2] Paolo Bonaiuti,[1] Stefano Villa,[3,6] Fabio Giavazzi,[3] Vittoria Matafora,[1] Angela Bachi,[1] Luca L. Fava,[4] Tiziana Lischetti,[1,*] and Andrea Ciliberto[1,5,7,*]

[1]IFOM ETS – The AIRC Institute of Molecular Oncology, Via Adamello 16, 20139 Milano, Italy
[2]ImmunoConcEpT, CNRS UMR5164, Université de Bordeaux, 33076 Bordeaux, France
[3]Dipartimento di Biotecnologie Mediche e Medicina Traslazionale, Universitá degli Studi di Milano, 20090 Segrate, Italy
[4]Armenise-Harvard Laboratory of Cell Division, Department of Cellular, Computational and Integrative Biology – CIBIO, University of Trento, Trento, Italy
[5]Pázmány Péter Catholic University, Faculty of Information Technology and Bionics, 1083 Budapest, Hungary
[6]Present address: Max Planck Institute for Dynamics and Self-Organization, Göttingen, Germany
[7]Lead contact
*Correspondence: mattia.pavani@ifom.eu (M.P.), tiziana.lischetti@icloud.com (T.L.), andrea.ciliberto@ifom.eu (A.C.)
https://doi.org/10.1016/j.celrep.2023.112215

SUMMARY

Drugs targeting microtubules rely on the mitotic checkpoint to arrest cell proliferation. The prolonged mitotic arrest induced by such drugs is followed by a G1 arrest. Here, we follow for several weeks the fate of G1-arrested human cells after treatment with nocodazole. We find that a small fraction of cells escapes from the arrest and resumes proliferation. These escaping cells experience reduced DNA damage and p21 activation. Cells surviving treatment are enriched for anti-apoptotic proteins, including Triap1. Increasing Triap1 levels allows cells to survive the first treatment with reduced DNA damage and lower levels of p21; accordingly, decreasing Triap1 re-sensitizes cells to nocodazole. We show that Triap1 upregulation leads to the retention of cytochrome *c* in the mitochondria, opposing the partial activation of caspases caused by nocodazole. In summary, our results point to a potential role of Triap1 upregulation in the emergence of resistance to drugs that induce prolonged mitotic arrest.

INTRODUCTION

Drugs that affect microtubule dynamics arrest cells in mitosis by activating the mitotic checkpoint (or spindle assembly checkpoint [SAC]).[1] This is a surveillance mechanism which guarantees that cells undergo anaphase only when all microtubules are properly attached to kinetochores. The SAC is activated during every cell division cycle in higher eukaryotes, thereby setting the pace of normal mitotic duration. In normal conditions, this activation lasts for short times. In contrast, the mitotic checkpoint can be activated for much longer by drugs that alter microtubule/kinetochore attachments. This is the case, for example, of drugs that impair microtubule dynamics such as taxol or nocodazole. Upon the effect of these drugs, cells suffer a prolonged arrest in mitosis from which they can escape thanks to the slow but constant degradation of cyclin B which takes place regardless of an active mitotic checkpoint.[2,3] Cells undergoing this process are said to "slip" through the arrest when cyclin B levels are so low that cannot sustain a mitotic arrest.[2–4] However, some cells do not escape but rather undergo apoptosis and die. The mechanism of cell death under mitotic arrest is less understood, and triggered by multiple parallel pathways.[5–8] A "death timer" based on the checkpoint-independent degradation of Mcl-1 has been identified.[9,10] Mcl-1 is an anti-apoptotic

factor, which prevents cytochrome *c* release from mitochondria and thus apoptosis.[5,11,12] Hence, both cyclin B and Mcl-1 degradation occur during mitosis and direct cells toward opposite fates. The presence of two thresholds has been hypothesized, one for slippage and one for apoptosis: depending whether cells cross the death threshold or the mitotic exit threshold first, they will either die or slip out of mitosis. This "competing network model" greatly helped in rationalizing and predicting cell fate upon drug treatment.[2]

Cells that survive the prolonged arrest are blocked in the next G1-phase.[4,13–15] The arrest is due to a mitotic clock, which stops cells in the next G1 for any extension of mitosis that exceeds 1.5 h.[16] This pathway relies on p53, 53bp1, and Usp28, it responds to centrosome loss, extended mitotic arrest but not necessarily to DNA damage.[17–19] However, DNA damage and DNA damage response were also reported during prolonged mitotic arrest,[7,14,15,20,21] caused by a partial apoptotic response,[7,20] and by telomere deprotection.[21] p53 was activated in consequence of the damage, and played a fundamental role to maintain the G1-arrest.[14,16,20] Finally, aberrant nuclei were observed as a consequence of slippage or treatment with nocodazole.[14,22,23]

Sub-lethal activation of the apoptotic pathway during a mitotic arrest, was shown to cause DNA damage by the partial release of cytochrome *c* from mitochondria, resulting in caspase-activate
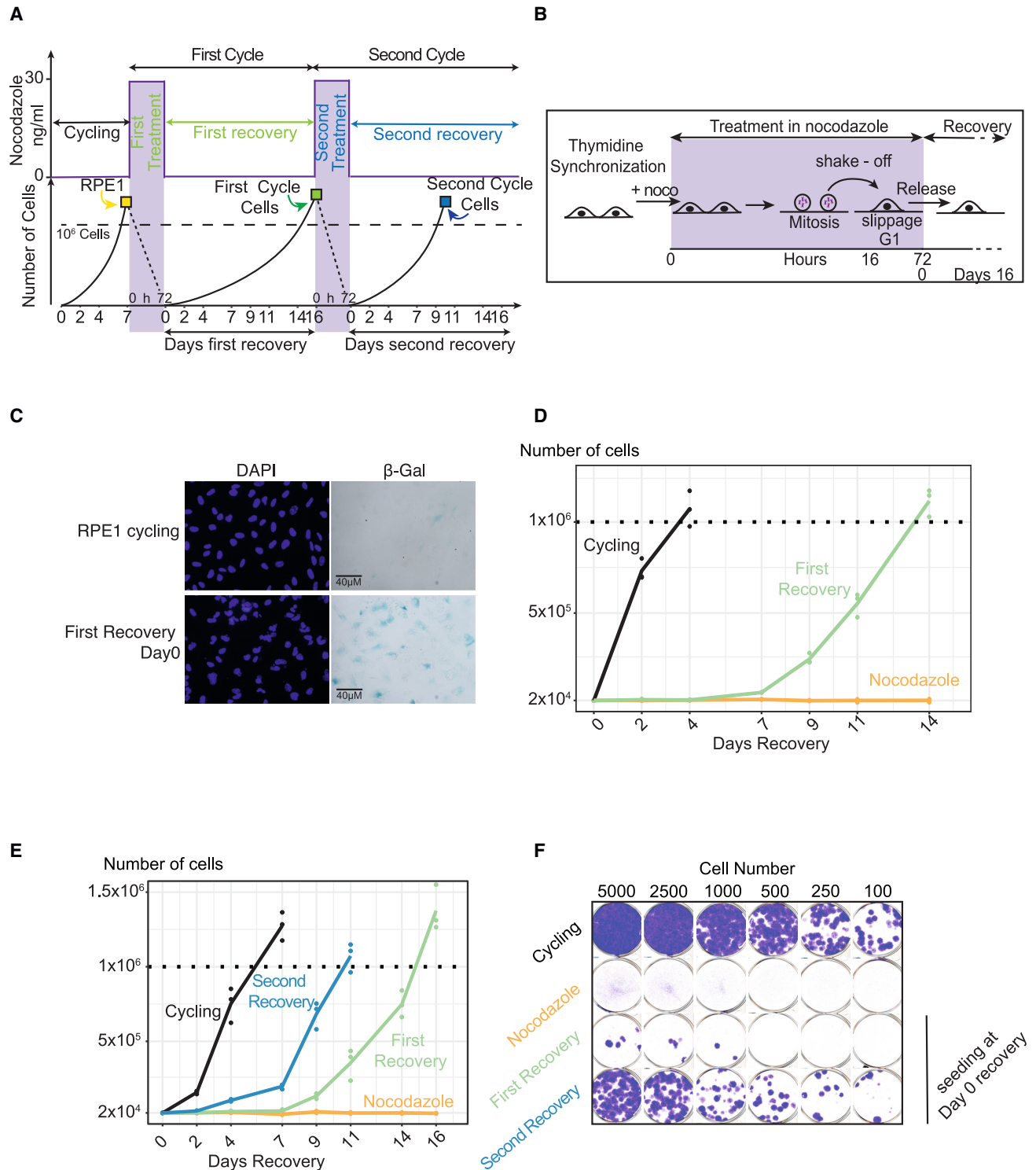
Figure 1. Cells escape from senescence induced by mitotic slippage, and those surviving one treatment recover faster from a second treatment

(A and B) Experimental setting.

(A) The full protocol consists of two treatments with nocodazole at 100 nM (shown in purple), and two recoveries from nocodazole—altogether two cycles. Treatments lasted 72 h, while recoveries lasted 16 days. At the end of each recovery, cells resumed exponential growth and reached confluence (dashed line). At this point, they were collected and stored. The first cycle, starting from RPE1 cells, produced first-cycle (FC) cells. The second cycle, starting from FC cells,

(legend continued on next page)

DNase activation.[20,24] Indeed, DNA damage following mitotic arrest can be decreased by inhibiting caspases, but also increased by targeting antiapoptotic factors such as Bcl-2 and Bcl-x.[7,20] Proteins preventing cytochrome *c* loss from mitochondria have been identified, among them Tp53 regulated inhibitor of apoptosis 1 (Triap1).[25] The expression of this protein is under the control of p53, and, surprisingly, it dampens canonical p53 outputs: Triap1 inhibits both p21-dependent cell-cycle arrest and apoptosis.[26,27] Triap1 expression correlates with poor prognosis in melanoma and renal cancer patients, as found in Human Protein Atlas database (TGCA). Coherently, Triap1 overexpression has been implicated in progression of nasopharyngeal cancer[28] and leads to doxorubicin resistance in MCF7 breast cancer cell lines.[29] So far, no role for Triap1 during prolonged mitotic arrest has been reported.

While several studies have elucidated the short-term consequences of prolonged mitotic arrest,[14–16,18,19,30] less attention has been devoted to understanding the long-term fate of cells that survive abnormal mitosis. The assumption is that they are irreversibly arrested in the cell cycle, in a senescence-like state which depends on p53 and p21.[20,30,31] Their permanent arrest in the cell cycle is regarded as tumor suppressive.[6] However, so far studies have not explored the possibility that in the long term some cells may be able to resume proliferation. Escape from cell-cycle arrest after drug treatment is relevant in the context of cancer. Cells that start proliferating again have escaped safeguard mechanisms, and are likely to have developed genetic abnormalities. Hence, we were interested in understanding whether cells are irreversibly arrested after slippage-induced prolonged mitotic arrest.

We find that a small fraction of cells surviving slippage resumes cell proliferation, and gives rise to a new population of cells that recovers faster from a second treatment. We show that this phenotype requires the upregulation of Triap1.

RESULTS

Cells escape from a G1 arrest caused by slippage in nocodazole

We asked what happens on the long-run to cells that undergo mitotic slippage. We developed a protocol (Figure 1A) that combines short-term manipulation to enrich our population with cells that have undergone slippage (we call this step "treatment," Figure 1B); and long-term observation of cells after treatment (we call this phase "recovery"). We refer to the combination of treatment and recovery as one "cycle." Treatment with nocodazole lasted for 72 h, and recovery from slippage in nocodazole for 17 days. The nocodazole concentration we used (100 nM) did not completely abrogate microtubule polymerization (Figure S1A), yet was sufficient to induce loss of spindle functionality resulting in prolonged mitotic arrest (Figure S1B), as shown by the localization of the checkpoint component Mad1 at kinetochores (Figure S1A). The fraction of polyploid cells after treatment was minimal (Figure 3A).

As expected, cells that survived treatment were arrested and largely senescent, ∼90% of them being positive to SA β-galactosidase (senescence-associated β-galactosidase) (Figure 1C). Surprisingly, after 7 days cells resumed proliferation giving rise to an exponentially dividing population, Figure 1D. We collected these cells (first-cycle cells, or FC cells), with the aim of analyzing them as shown in the next sections.

In summary, our data show that cells can escape from the G1 arrest induced by prolonged mitotic arrest and slippage and resume unhindered cell treated with nocodazole are de-sensitized to a second round of treatment

We reasoned that cells that had managed to escape from the arrest may be less sensitive to a second round of treatment with nocodazole. Hence, we re-treated FC cells with nocodazole. After washing out the drug, these cells were also arrested in G1, the majority of them being positive for SA β-galactosidase (Figure S1C). Again, G1-arrested cells resumed proliferation (second recovery). Remarkably, they did so after a shorter period (less than 4 days) compared with the first recovery, Figure 1E. When these cells also grew exponentially, we collected them for further analyses (second cycle, or SC cells).

Besides the delay, growth during the two recoveries did not show major differences, with cells dividing only slightly faster after the second treatment (Figure S1D left, bulk). The shorter delay observed after the second treatment could be due to a larger fraction of cells recovering growth. To confirm this possibility, we performed a colony formation assay with cells seeded at the beginning of recovery. Results showed that indeed a larger fraction of cells divided after the second treatment than after the first (Figure 1F) (∼40/1,000 and ∼1/1,000, respectively).

To confirm that the observed behavior was not specific to RPE1 cells, we performed a similar experiment with the human immortalized fibroblast cell line BJ. We observed a similar reduced delay after one round of treatment (Figure S1E).

produced second-cycle (SC) cells. Throughout the text we compared cells that had stably recovered growth with cells that never experienced treatment (i.e., FC or SC cells vs. RPE1 before treatment); and we compared cells while they were experiencing treatment and recovery (i.e., first cycle vs. second cycle).

(B) RPE1 cells were synchronized in S-phase by a single thymidine block for 24 h. Cells were released in nocodazole (purple), mitotic cells were collected by shake-off after 16 h and replated in nocodazole for another 56 h to allow them to exit mitosis. Cells were kept in nocodazole for a total of 72 h, when they were released in fresh medium without drugs.

(C) Cells were treated with nocodazole as shown in (A) and (B) (first treatment). At recovery day 0, cells were fixed and stained for SA-β galactosidase. A total of 2.8% (n_{cells} = 141; N = 2) of RPE1 cells were positive for SA-β galactosidase, while 89.7% of cells were SA-β galactosidase positive after the treatment with nocodazole (n_{cells} = 146; N = 2). Scale bar, 40 μm.

(D) Cells derived from the first treatment (2 × 10^4) were plated in 6-well plates. Cells for each condition were counted in triplicate every 2/3 days until confluence (dashed line). The lines connect the average of three technical replicates (dots). N = 6. See also Figure S1.

(E) Cells derived from the first or second treatment (2 × 10^4) were plated in 6-well plates. Cells for each condition were counted in triplicate every 2/3 days until confluence (dashed line). The lines connect the average of three technical replicates (dots). N = 6.

(F) Cells derived from the first or second treatment were seeded at the indicated cell number on day 0, and stained with crystal violet on day 14. N = 3. See also Figure S1.
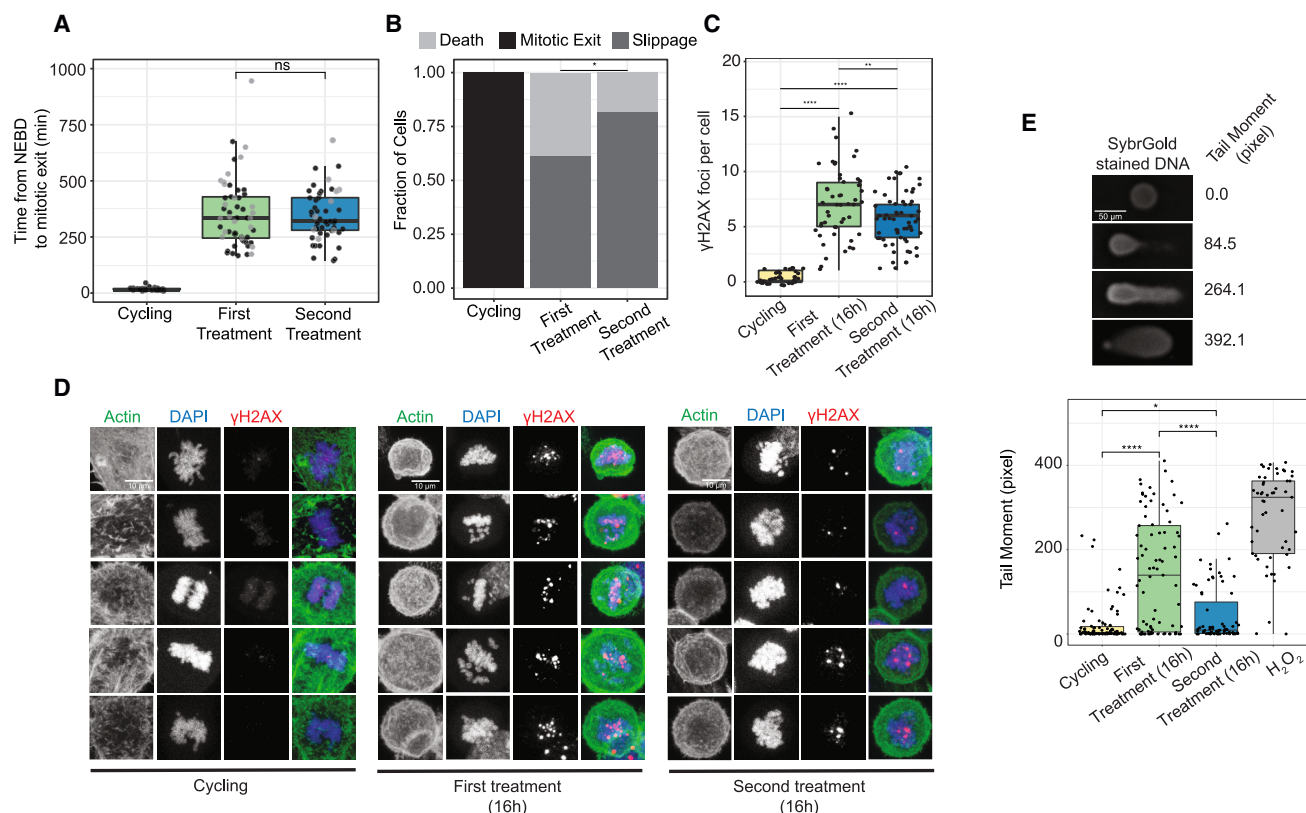
Figure 2. DNA damage and cell death decrease during the second treatment

(A) Cells were synchronized with double thymidine block and released in 100 nM nocodazole. Mitotic duration was measured from NEBD to cell re-adhesion using live-cell imaging. Gray dots represent cells that, by visual inspection, die during or immediately after mitotic slippage (see Figure S2). The boxes span the interquartile range (IQR) (from the 25th to the 75th percentiles), and the central band represents the median. The lower (upper) whisker extends from the box to the smallest (largest) value no further than 1.5*IQR from the box (n_{cells} = 47, 72, 69; N = 2). Kruskal-Wallis test was implemented (ns: p > 0.05).

(B) Data from the experiment shown in (A). In black, cells that underwent normal mitotic exit. In dark gray, cells that survived slippage (equivalent to black dots in (A)). In light gray, cells that died during or immediately after mitotic slippage (equivalent to gray dots in A). The Fisher's test was implemented (*p ≤ 0.05). Representative images of each category are reported in Figure S2.

(C) Quantification of immunofluorescence on γH2AX in mitotically arrested cells. Cells were synchronized in S-phase and released in nocodazole for the first or second cycle (protocol as in Figure 1B). After 16 h, cells were fixed; DNA was stained with DAPI. The boxes span the interquartile range (IQR) (from the 25th to the 75th percentiles), and the central band represents the median. The lower (upper) whisker extends from the box to the smallest (largest) value no further than 1.5*IQR from the box (n_{cells} = 55, 60, 63; N = 2). Kruskal-Wallis test was implemented (**p ≤ 0.01, ****p ≤ 0.0001).

(D) Raw confocal images quantified in (C). Scale bar, 10 μm.

(E) Comet assay of cells under nocodazole arrest, during the first and second treatment. Mitotic cells were collected by shake off 16 h after thymidine release. Cycling cells were used as negative control, and cells treated with H_2O_2 as positive control. The extent of DNA damage was measured by the tail moment, defined as tail length times the percent of tail DNA. Scale bar, 50 μm. The boxes span the IQR (from the 25th to the 75th percentiles), and the central band represents the median. The lower (upper) whisker extends from the box to the smallest (largest) value no further than 1.5*IQR from the box (n_{cells} = 82, 81, 71, 53; N = 3). Kruskal-Wallis test was implemented (*p ≤ 0.05, ****p ≤ 0.0001). See also Figure S2.

We conclude that cells capable of surviving slippage are selected for some features that allow them to more efficiently survive a second treatment with the same drug.

DNA damage and cell death decrease in consequence of the second treatment

To understand the different recovery times after one or two treatments, we looked at differences during the period of treatment with nocodazole. First, we asked whether cells recovering faster had undergone a shorter mitotic arrest in the presence of nocodazole. We compared the time elapsed between nuclear envelope breakdown (readout of mitotic entry) and cell re-adhesion (readout of mitotic exit). Results show that cells were equally capable of mounting an efficient mitotic arrest after one or two cycles (Figure 2A). We then scored by visual inspection cells that survived slippage and those that did not (Figure S2). The fraction of dead cells decreased after the second treatment, matched by an increase in cells surviving slippage (Figure 2B).

The decrease in cell death may correlate with decreased DNA damage. Thus, we looked at DNA damage during treatment. Twenty-four hours after addition of nocodazole, we detected
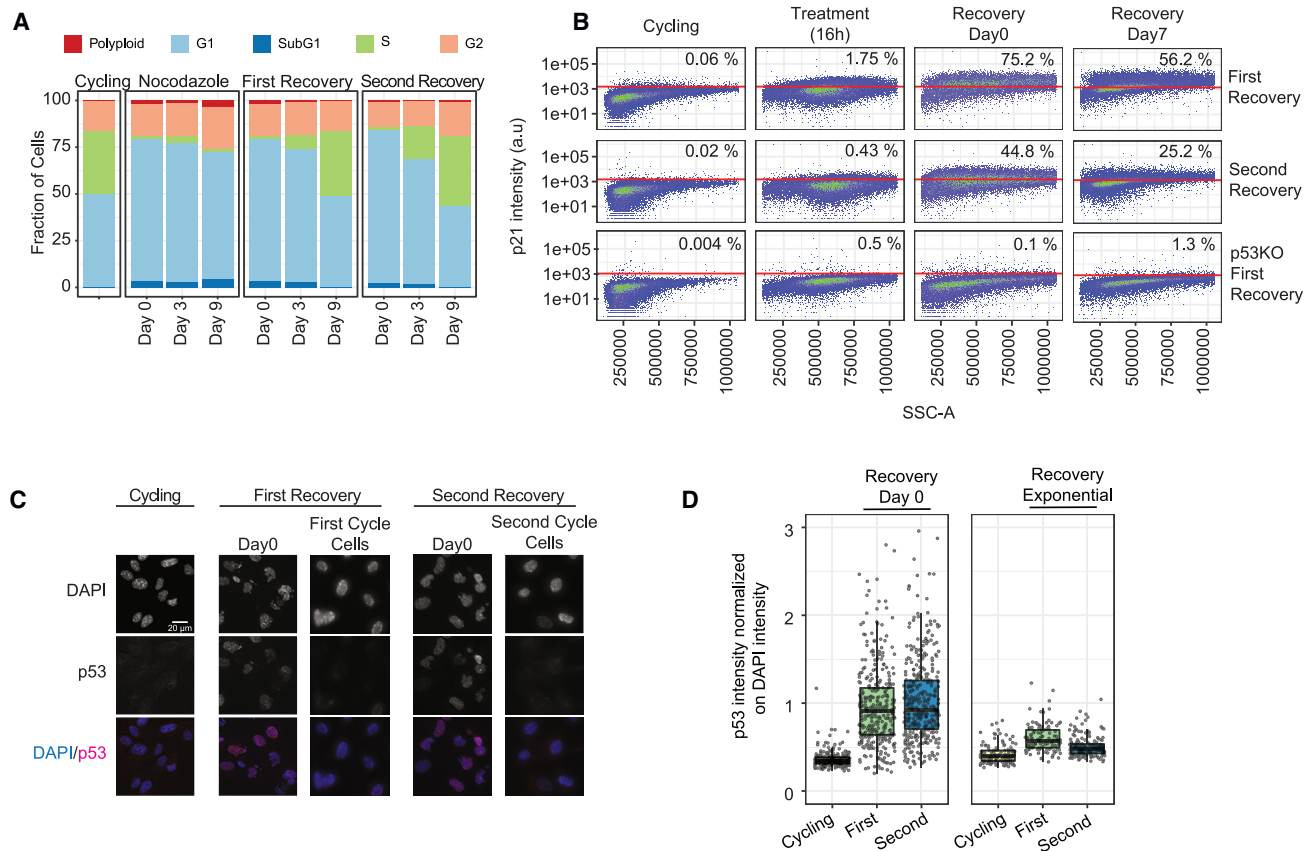
Figure 3. The second treatment produces a smaller fraction of p21-positive cells

(A) Cells were treated with the protocol shown in Figures 1A and 1B. At the indicated days they were pulsed with bromodeoxyuridine (BrdU) for 20 min and fixed. Cell-cycle stages were determined considering both propidium iodide (PI) labeling (G1, G2-M) and BrdU incorporation (S-phase). FACS profiles are reported in Figure S3A. N = 2.

(B) Cells were treated with the protocol shown in Figures 1A and 1B. p21-positive events were gated on singlet events. Cycling samples were collected from exponentially growing populations for each cell line. N = 3.

(C) Cells were treated with the protocol shown in Figures 1A and 1B and fixed at recovery day 0 or when they had restored exponential growth. Scale bar, 20 μm. p53 was immunostained, DNA was stained with DAPI.

(D) Quantification of p53 signal in (C). Nuclear p53 signal was determined by designing a ROI on the DAPI signal and p53 intensity was normalized on DAPI. The boxes span the interquartile range (IQR) (from the 25th to the 75th percentiles), and the central band represents the median. The lower (upper) whisker extends from the box to the smallest (largest) value no further than 1.5*IQR from the box ($n_{cells\ Day\ 0\ recovery}$ = 296, 429, 382; $n_{cells\ Recovery\ exponential}$ = 125, 113, 125; N = 3). See also Figure S3.

by immunofluorescence γH2AX foci in mitotically arrested cells. The number of foci, a marker of DNA damage response, suggests that nocodazole treatment induced DNA damage, in agreement with previous reports.[14,15,20] Interestingly, cells showed fewer foci during the second treatment (Figures 2C and 2D), and thus a lower amount of DNA damage response, compared with the first treatment. To confirm that decreased DNA damage response matched decreased DNA damage, we performed comet assays, where the tail moment is a measure of damage. Results showed that cells experienced reduced damage after the first cycle compared with the second cycle (Figure 2E).

In summary, we observed decreased cell death and DNA damage during the second treatment compared with the first, despite cells displaying an identical ability to mount a mitotic checkpoint response during both treatments.

Reduction in p21 levels underlies the faster recovery after the second treatment

We then analyzed cells during the first and second recovery phase. When we looked at the distribution of cell-cycle stages in different days during the recovery period, we observed, as expected, that cells were primarily arrested in G1. This was the case after both treatments. Compared with the first treatment, the fraction of cells in S-phase increased during the second treatment (Figures 3A and S3A). This is in agreement with a shorter arrest.

p21 plays a fundamental role in maintaining the G1 arrest after a prolonged mitotic arrest.[16,19,20] Thus, we examined p21-positive cells at different time points of our protocol: before treatment, during treatment, and at two different time points during recovery. As negative control, we used p53KO cells[32] lacking the p53-dependent induction of p21. Results show that, both

during the first and second cycles, the levels of p21 increased, reached a plateau, and decreased. Interestingly, we observed that, at every time point, p21-positive cells reached lower levels after the second treatment than after the first (Figure 3B). In agreement with the arrest being p53 dependent, we observed that p53KO cells displayed a much reduced delay after treatment compared with FC cells (Figure S3B).

Given that p21 dynamics following stress depends on p53, we also looked for differences in p53 accumulation between the two cycles. We observed p53 localization at the beginning of recovery by immunofluorescence, which was much reduced when cells had resumed growth (Figures 3C and 3D), but we did not detect major differences by IF between first and second treatment. This result does not explain the decrease in p21-positive cells observed after the second treatment, which may be due to changes in p53 activity.

As a different approach to understand whether cells selected by treatment have an altered p53 response following mitotic arrest, we challenged FC and SC cells with centrinone. This is a drug that prevents centrosome duplication and thereby elicits the 53BP1-USP28-p53 pathway.[17–19] By western blotting, we detected p21 and p53 levels. We did not observe relevant differences among FC, SC and RPE1 cells (Figure S3C).

Instead, we noticed a relevant change concerning nuclear shape. Compared with normal cycling RPE1 cells, we observed deformed and fragmented nuclei at the beginning of the first recovery. When cells reached exponential growth (FC cells), both deformation and fragmentation decreased, becoming more similar to that of untreated RPE1 cells in exponential growth (Figure S3D). At the beginning of the second recovery cells had milder nuclear defects and their nuclear morphology appeared similar to that of untreated RPE1 cells.

In conclusion, cells undergo a p53-dependent G1 arrest during the recovery period. After both treatments, we observed an efficient p53 response, and we confirmed the presence of an intact 53BP1-USP28-p53 pathway. Yet, the expression of p21 decreased between the first and second treatments, in parallel with reduced DNA damage. Decrease of p21 correlated with more physiological nuclear morphology.

Triap1 is upregulated in response to slippage

To gain insights on the molecular mechanisms selected by treatment with nocodazole, we analyzed the proteome of FC and SC cells, as opposed to cells before treatment. After PCA, untreated cells and cells treated once or twice clustered together as expected (Figure S4A). We identified proteins that were up- or downregulated both in FC and SC cells (Figures 4A and 4B). Within this set of proteins, several pathways were enriched (Figure 4C; Table S1). In particular, we observed that proteins involved in apoptosis were enriched among the significantly changing proteins (Figure 4B; Table S2). Given the reduction of cell death between first and second treatments, we focused on this class, and in particular on Triap1, which showed the second highest fold change within this class. This was not due to increased Triap1 stability, which does not change in FC cells (Figure S4B). Rather, the fact that Triap1 mRNA levels were increased points to an increase of protein production (Figure 4D).

To confirm the generality of Triap1 upregulation after treatment, we tested the expression levels of the protein in hTERT-immortalized BJ cells, where recovery is shorter after the second treatment (Figure S1E). We found that Triap1 was upregulated after treatment in this cell line as well (Figure 4E).

Exponentially dividing FC and SC cell lines maintain their properties (i.e., fast recovery post-slippage) after many generations without selective pressure. Hence, we hypothesized that Triap1 upregulation may be caused by genetic changes, the most plausible of them being aneuploidy, given the increased missegregation upon treatment with nocodazole. We sequenced FC cells with low coverage, and looked for changes in chromosomes number. Yet, we did not detect any specific aneuploidy or major structural changes except for the loss of chrXII arm duplication (Figure S4C), where we did not identify genes that could explain Triap1 upregulation.

To understand whether Triap1 upregulation was due to some pre-existing mutation in the population, we repeated the treatment shown in Figures 1A and 1B on single clones. The results were in line with what we observed in bulk: similar growth rates (Figure S1D, left), anticipated recovery after one treatment (Figure S1D, right), and increased Triap1 protein levels after treatment (Figure S4D). In summary, these data do not support the hypothesis of pre-existing mutations. They leave open the possibility that epigenetic changes (i.e., phenotypic reversible changes not due to alterations of DNA sequences) underlie Triap1 upregulation.

In conclusion, after treatment with nocodazole we selected cells that had altered expression of anti-apoptotic players, including Triap1. The upregulation of Triap1 occurs both at the level of mRNA and protein, and relies neither on aneuploidy nor on pre-existing mutations.

Triap1 overexpression desensitizes cells to nocodazole

We then tested whether changes in expression of Triap1 were causal of, or merely correlative with, the phenotypes observed following slippage. To this aim, we overexpressed Triap1 in cells before treatment; and we downregulated it in FC cells (Figures 5A and 5B). In the first case, we expected to mimic treatment in cells that were never treated; in the second we expected to revert cells that were treated to the state of untreated cells.

To increase Triap1 levels, we expressed it under the constitutive CMV promoter (Triap1 OE cells). The fold change increase for both mRNA (Figure 5C) and proteins (Figure 5D) were higher but in the same range—around 2-fold—of that observed in FC cells. In untreated cells, the increased expression levels did not show any effect on growth rate (Figure S5A), and the protein localized in mitochondria both in interphase and mitosis, as expected (Figure S5B). Interestingly, Triap1 OE cells after the first treatment of nocodazole resumed growth already after 4 days (Figure 5E), similar to RPE1 cells that had gone once through slippage in nocodazole (Figure 1E).

To lower the levels of Triap1, we silenced gene expression with shRNA (Triap1 KD cells) (Figure 5F). The knockdown performed in FC cells did not show any phenotype in terms of growth (Figure S5C). When we followed the protocol described in Figure 5B, however, the phenotype of Triap1 KD cells resembled that of untreated cells: after a second round of treatment cells recovered
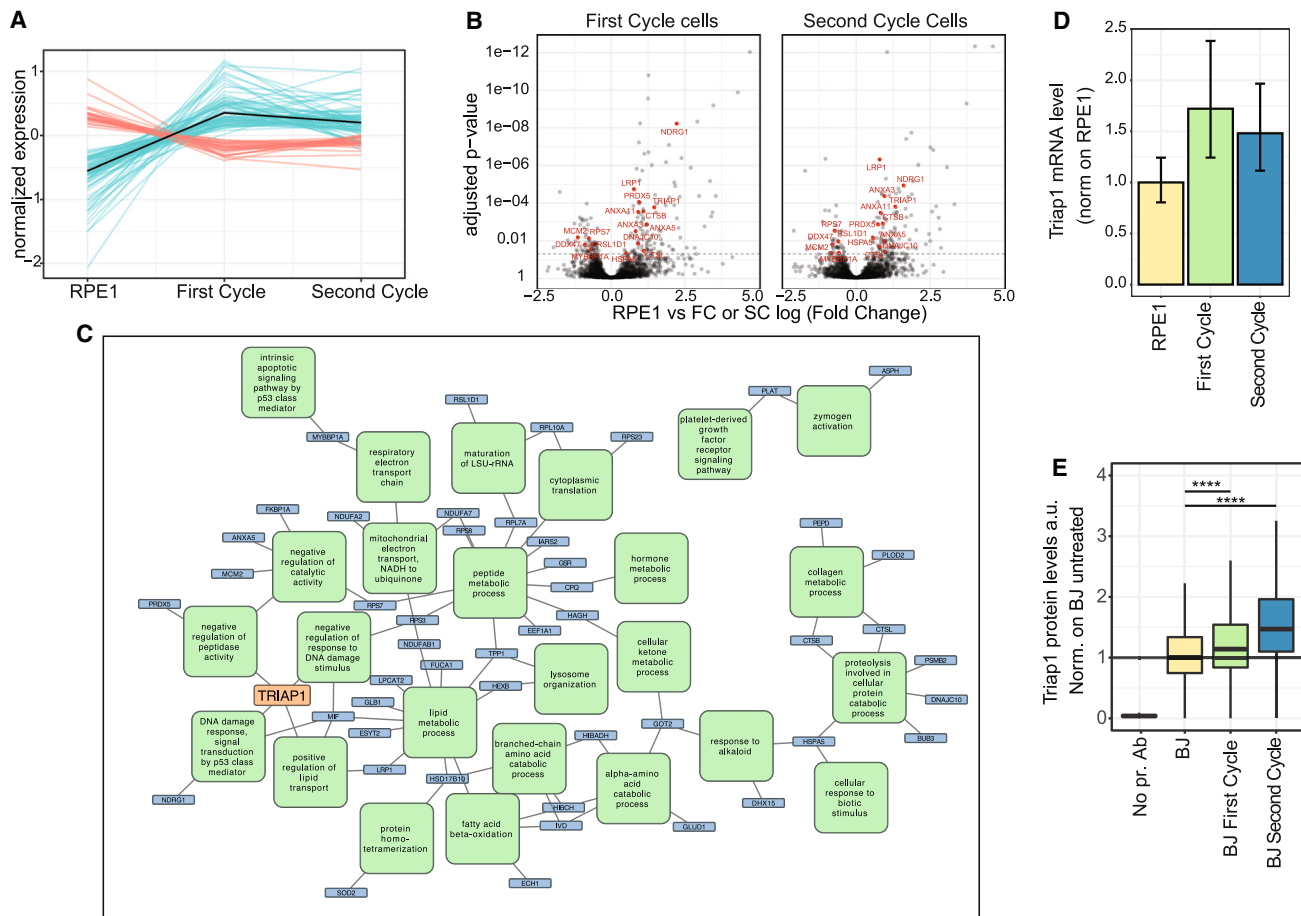
Figure 4. Mass spectrometry reveals altered levels of Triap1 after treatments with nocodazole

(A) Proteins significantly up- and downregulated in both SC and FC cells compared with cycling RPE1 cells. For each biological replicate (N = 3) two technical replicates were produced.

(B) Volcano plot of differences for all proteins (gray dots) between cycling RPE1 and either first-cycle cells (left) or second-cycle cells (right). Highlighted in red are proteins related with apoptosis (see STAR Methods) with an adjusted p value below 0.05 (dashed line).

(C) The graph depicts the connections between the significant genes and significant GO terms (Tables S1 and S2). Proteins that were not connected to any of the significant terms were omitted from the graph.

(D) Triap1 mRNA levels in cycling cells (RPE1, FC, and SC). For each sample, Triap1 cDNA level was normalized on GAPDH cDNA. Bars height represent the RQ from 5 technical replicates (N = 3), whiskers represent the 95% confidence interval.

(E) Triap1 protein abundance was determined by FACS intracell staining. hTERT-BJ FC and SC cells were produced following the protocol in Figures 1A and 1B. The boxes span the interquartile range (IQR) (from the 25th to the 75th percentiles), and the central band represents the median. The lower (upper) whisker extends from the box to the smallest (largest) value no further than 1.5*IQR from the box. N = 2. Kruskal-Wallis test was implemented (****p ≤ 0.0001). See also Figure S4.

growth only after 7 days of arrest (Figure 5G). Using a different shRNA for Triap1 validated in Andrysik et al.[26] we obtained the same results (not shown).

Finally, we asked whether other macroscopic phenotypes associated with treatment could be reproduced or reverted by Triap1 up- and downregulation. This was the case for colony formation assays, where Triap1 OE cells showed an increased number of colonies compared with EV cells, in line with that observed after the second treatment (Figure S5D). The number of colonies observed in Triap1 KD cells, instead, decreased compared with the control, similarly to that seen in cells after the first treatment (Figure S5E). Also nuclear morphologies were well recapitulated by overexpressing Triap1 levels (Figure S5F).

In conclusion, we showed that modulating the levels of Triap1 in cells before or after treatment is sufficient to recapitulate or reverse key phenotypes observed in cells recovering from slippage.

Triap1 overexpression reduces DNA damage and p21 expression by inhibiting cytochrome *c* release

We then addressed how Triap1 overexpression may impact on recovery after treatment. Data presented above show that, during the second treatment, RPE1 cells reduced DNA damage response, DNA damage, and the number of p21-positive cells (Figures 2C, 2E, and 3B, respectively). When we repeated the experiment with Triap1 OE cells, we observed a similar behavior: decreased damage (Figure 6A), reduced number of γH2AX foci
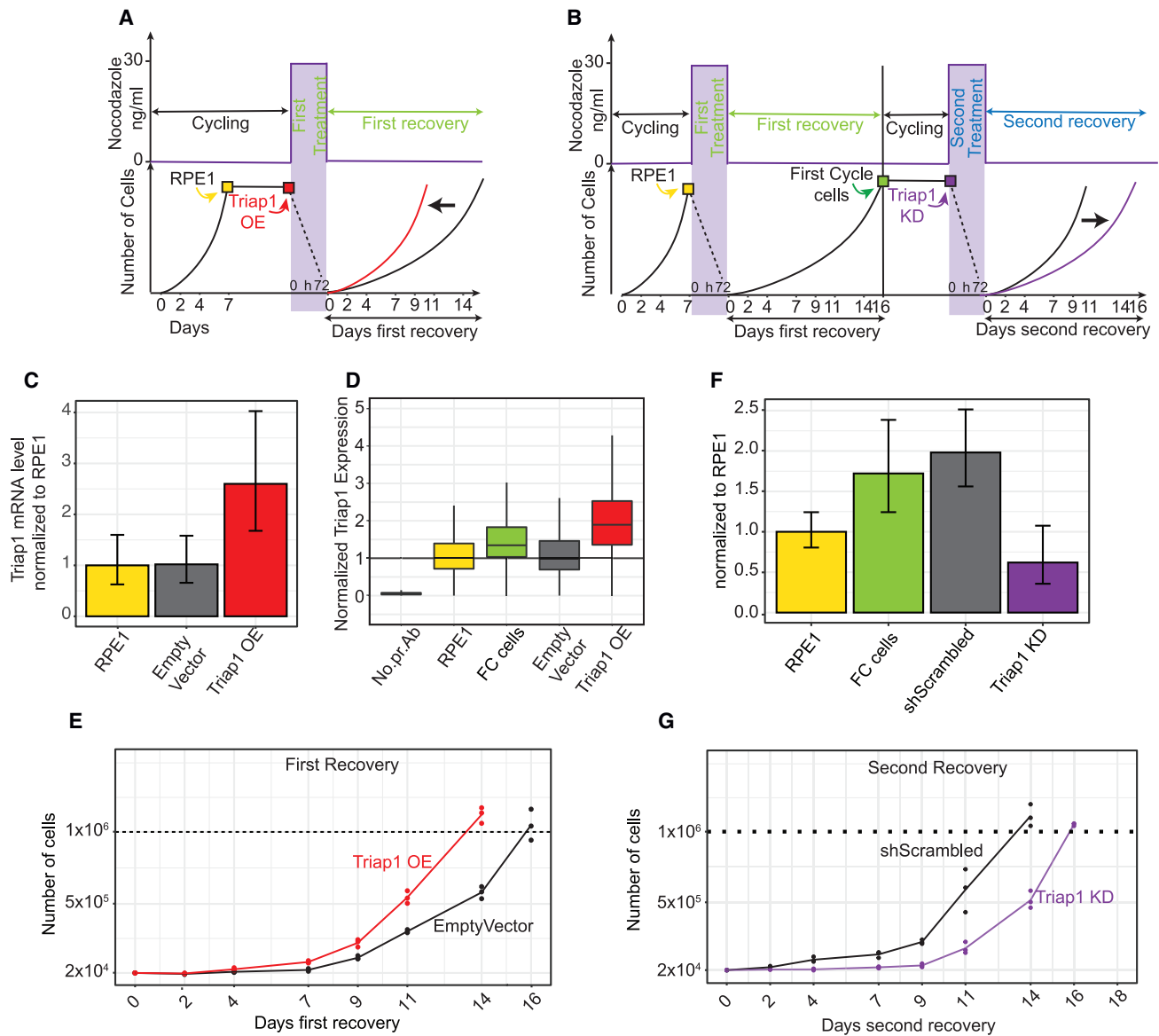
Figure 5. Triap1 upregulation recapitulates the first cycle of treatment, while Triap1 downregulation resets it

(A and B) Protocol design to obtain Triap1 OE (A) and Triap1 KD cells (B). Triap1 overexpression was performed in RPE1 cells growing exponentially, while Triap1 KD was implemented on FC cells. Growth was assessed starting from day 0 of recovery. Nocodazole treatment is depicted in purple.

(C) Triap1 mRNA abundance in RPE1, empty vector, and Triap1 OE. Total mRNA was retrotranscribed in cDNA from cycling cells. For each sample, Triap1 cDNA level was normalized on GAPDH cDNA. Bar heights represent the RQ from five technical replicates, whiskers represent the 95% confidence interval. N = 3.

(D) Triap1 protein abundance in RPE1, FC, empty vector, and Triap1 OE. Triap1 protein expression was determined by FACS intracell staining. A total of 83% of Triap1 OE cells showed Triap1 levels higher than the median of empty vector cells. Distributions were obtained from 3 (FC) or 2 (Triap1 OE) biological replicates. The boxes span the interquartile range (IQR) (from the 25th to the 75th percentiles), and the central band represents the median. The lower (upper) whisker extends from the box to the smallest (largest) value no further than 1.5*IQR from the box.

(E) Following the protocol in (A) (first recovery), 2×10^4 cells derived from Triap1 OE were plated in 6-well plates. Cells for each condition were counted in triplicate every 2/3 days until the confluence of the 6 wells had been reached (dashed line). The line connects the average of three technical replicates (dots). N = 2.

(F) Triap1 mRNA abundance in RPE1, FC, shScrambled, and Triap1 KD cells. Total mRNA was retrotranscribed in cDNA from cycling cells. For each sample, Triap1 cDNA level was normalized on GAPDH cDNA. Bar heights represent the RQ from 5 technical replicates, whiskers represent the 95% confidence interval. N = 3.

(G) Following the protocol in (B) (second recovery), 2×10^4 cells derived from Triap1 KD were plated in 6-well plates. Cells for each condition were counted in triplicate every 2/3 days until the confluence of the 6 wells had been reached (dashed line). The line connects the average of the three technical replicates (dots). N = 4. See also Figure S5.

(Figure 6B), and less p21-positive cells (Figure 6C). When Triap1 OE were cycling, instead, there was no DNA damage compared with controls (Figures S6A and S6B).

Prolonged mitotic arrest causes DNA damage via sub-lethal release of cytochrome *c*, an effect that can be reversed by treatment with caspase inhibitors.[7,20] We asked whether Triap1 could play a similar role as such inhibitors. Hence, we first assessed whether treatment with nocodazole caused partial release of cytochrome *c*. While untreated cells showed a clear mitochondrial localization of cytochrome *c*, treatment with nocodazole caused its partial cytoplasmic release. This was less than that caused by hydrogen peroxide, but still detectable (Figure S7A).

We then compared cytochrome *c* release in cells overexpressing Triap1 as opposed to control cells. As a measure of delocalization, we used the coefficient of variation (i.e., mean divided by standard deviation) of cytochrome *c* signal, which was similar in untreated mitotic control cells (empty vector) and mitotic Triap1 OE (Figures 7A and 7B). Upon treatment with nocodazole, the coefficient of variation of mitotic control cells decreased due to the delocalization of cytochrome *c*. This effect was reduced in mitotic cells overexpressing Triap1 (Figures 7A and 7B). In agreement with the hypothesis that Triap1 upregulation reduces caspase activity, we observed that Triap1-overexpressing cells decreased cleaved caspase-3 levels and increased vitality measured as ATP molecules in the population (Figures S7B and S7C).

We then asked whether cytochrome *c* delocalization was also decreased when FC cells were treated with nocodazole a second time. This is what we observed (Figures S7D–S7F), although the decrease was more limited than in Triap1 OE, possibly due to the reduced Triap1 expression levels in FC cells compared with Triap1 OE cells (Figure 5D).

Finally, we reasoned that FC cells may be able to tolerate other treatments prone to cause cytochrome *c* release. To test this idea, we treated FC cells with doxorubicin, a topoisomerase 2 inhibitor that leads to DNA double-strand breaks and causes apoptosis. We used RPE1 cells as control. Cells were treated with different drug concentrations for 24 h, then released and monitored. Interestingly, after treatment with doxorubicin at 100 and 150 nM, FC cells recovered faster than RPE1 cells (Figure 7C).

We conclude that Triap1 upregulation decreases DNA damage by preventing cytochrome *c* release. The ability of cells overexpressing Triap1 to prevent apoptosis is not specific to nocodazole, as it can also be appreciated in FC cells after treatment with doxorubicin.

DISCUSSION

We treated untransformed cells with nocodazole, enriching the population with cells that undergo slippage. In agreement with previous results, we found that these cells accumulated DNA damage, expressed p21, and arrested in G1.[7,13,19,20] Unexpectedly, we observed that cells were not permanently arrested in the cell cycle. A small fraction (~1/1,000 cells) resumed proliferation, switched off p21 expression, and repaired DNA damage. When re-treated with nocodazole, they took a shorter time to resume cell proliferation compared with the first treatment. Upregulation of Triap1 elicited the same effect, including the reduction of DNA damage and reduced levels of p21. Our results are in agreement with data showing that prolonged mitotic arrest leads to DNA damage caused by sub-lethal activation of apoptosis,[7,20] and indeed Triap1 upregulation came with decreased cytochrome *c* delocalization. Hence, in our setting, high Triap1 levels may play a similar role as caspase inhibitors. In this sense, Triap1 may be part of the network controlling cell death in alternative to slippage, as hypothesized by the "networks competing model."[2]

The majority of cells arrested after slippage was positive for p21 and for the β-galactosidase assay. As such, we identified them as senescent cells. The identification of this escape route from senescent arrest, a known tumor-suppressor mechanism, is potentially important for understanding the limitations of chemotherapy. Interestingly, the process we describe may be not limited to treatment with nocodazole, since cells primed with nocodazole show decreased sensitivity to doxorubicin as well. The possibility that one type of mitotic arrest may desensitize cells to other treatments causing DNA damage may help to understand how cells develop cross-resistance to different drugs. We need to remark, however, that we cannot exclude the possibility that cells resuming cell division never entered senescence. In the future, it will be important to investigate the nature of cells resuming proliferation after slippage at the single-cell level.

Mechanisms of selection for cells capable of recovering growth

Our data suggest a role for Triap1 in the selection of cells capable of recovering growth, yet how cells overexpressing Triap1 may be selected is not clear. Triap1 is a substrate of p53, and is probably expressed in a large fraction of cells, since we observe p53 activity during treatment and early recovery. This complicates the simplest scenario whereby only cells that produce Triap1 are selected and escape the arrest. Likely more than 1/1,000 cells express Triap1 during treatment and recovery. Moreover, Triap1 counteracts the effects of p53. By decreasing DNA damage, it may well downregulate its own production. However, FC and SC cells (i.e., cells that have fully recovered growth and show little p53 levels) maintain their ability to recover fast from nocodazole treatment and show higher levels of Triap1. Hence, we hypothesize that treatment selects a subfraction of cells where Triap1 regulation is partially independent on p53. Possibly, this comes with stably higher values of Triap1 that give a selective advantage, because of decreased DNA damage (Figure 7D).

We also need to keep in mind that mass spectrometry data showed a high number of up- and downregulated proteins. It is very likely that other mechanisms and other molecular players contribute to the observed phenotypes besides increased Triap1 levels. Even considering just modulation of apoptosis, a whole subnetwork of anti-apoptotic proteins showed high and stable expression level. These results are in line with the idea that apoptosis is controlled by overlapping and redundant subnetworks. Myc, a key regulator of many of them,[5] was not detected by mass spectrometry. Additional experiments will be needed to test the presence of master regulators in controlling the expression of anti-apoptotic components.
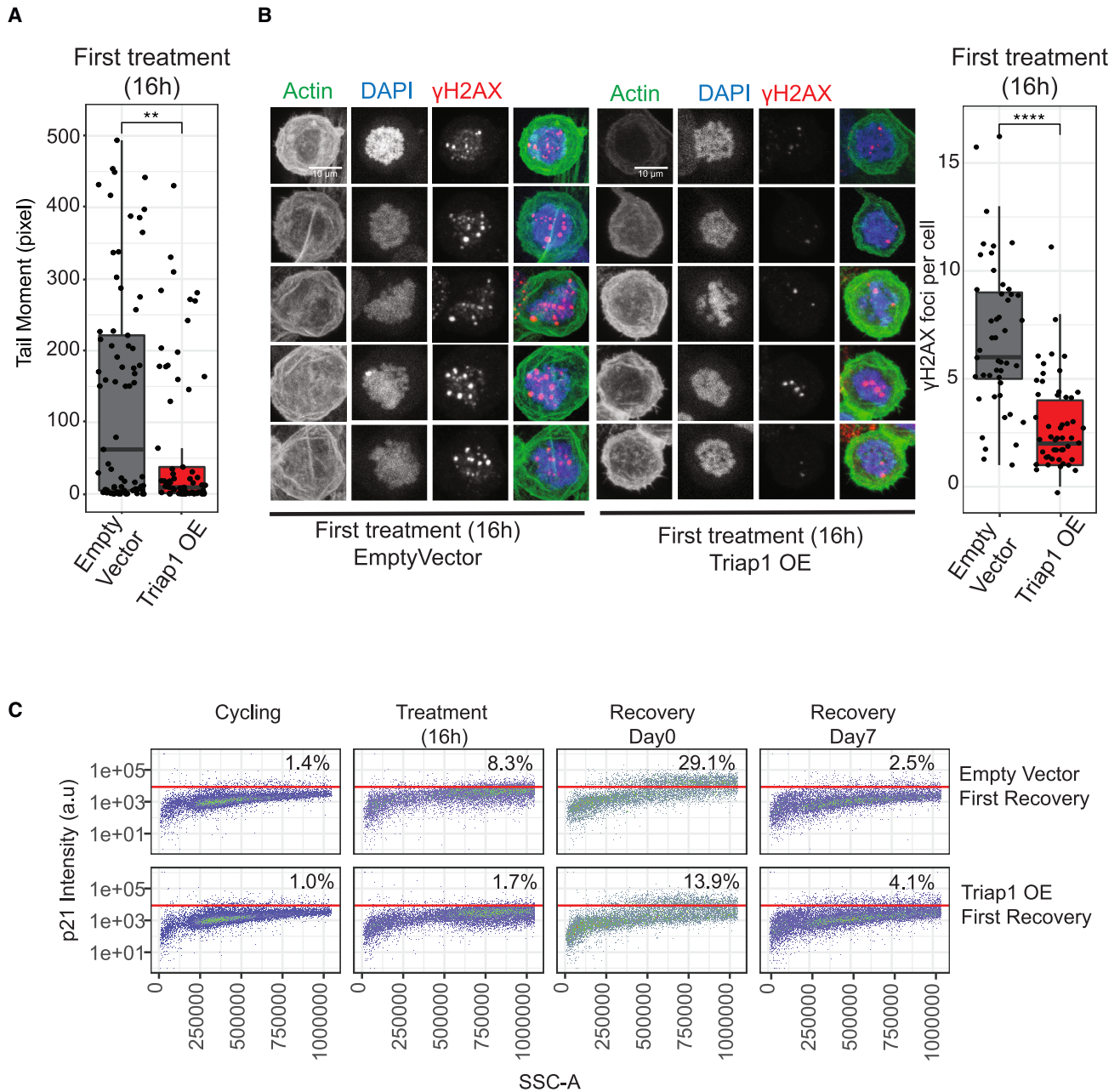
A

First treatment
(16h)

B

First treatment
(16h)

First treatment (16h)
EmptyVector

First treatment (16h)
Triap1 OE

C

Figure 6. Triap1 overexpression reduces DNA damage, apoptosis, and p21-positive cells

(A) Comet assay of cells under nocodazole arrest. Cells were treated as described in Figures 1A and 1B. Mitotic cells were collected by shake off 16 h after thymidine release. The extent of DNA damage was measured by the tail moment, defined as tail length times the percent tail DNA. The boxes span the interquartile range (IQR) (from the 25th to the 75th percentiles), and the central band represents the median. The lower (upper) whisker extends from the box to the smallest (largest) value no further than 1.5*IQR from the box (n_{cells} = 73, 79; N = 2). Kruskal-Wallis test was implemented (**p $\leq$ 0.01).

(B) Cells were treated as for the protocol in Figures 1A and 1B. After 16 h from nocodazole addition, cells were fixed and DNA was stained with DAPI. γH2AX foci were counted using a custom Fiji script. Scale bar, 10 μm. The boxes span the interquartile range (IQR) (from the 25th to the 75th percentiles), and the central band represents the median. The lower (upper) whisker extends from the box to the smallest (largest) value no further than 1.5*IQR from the box (n_{cells} = 65, 59; N = 2). Kruskal-Wallis test was implemented (****p $\leq$ 0.0001).

(C) Cells were treated as for the protocol in Figures 1A and 1B. p21-positive cells were detected by FACS, gating on singlet events. Cycling cells were collected from exponentially growing populations. N = 3. See also Figure S6.
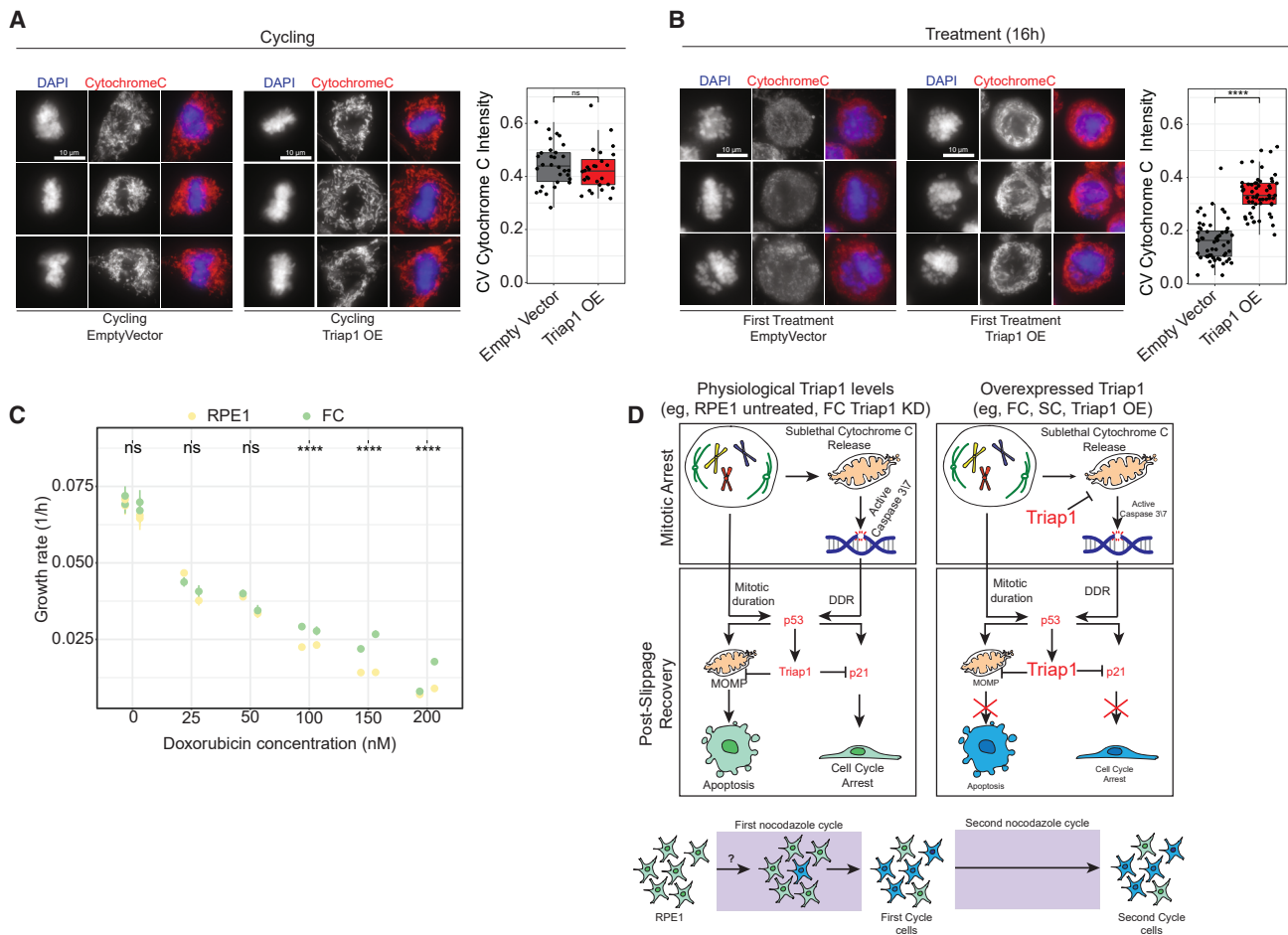
Figure 7. Altering Triap1 expression affects cytochrome *c* release during nocodazole treatment

(A and B) Cytochrome *c* localization in cycling cells (A) and in cells arrested in mitosis by nocodazole 16 h after thymidine release (B). Cytochrome *c* was immunostained. Scale bar, 10 μm. The coefficient of variation (CV) of cytochrome *c* signal was calculated, as described in STAR Methods, to evaluate protein localization. The boxes span the interquartile range (IQR) (from the 25th to the 75th percentiles), and the central band represents the median. The lower (upper) whisker extends from the box to the smallest (largest) value no further than 1.5*IQR from the box ($n_{cells\ panel\ A}$ = 30, 28, $n_{cells\ panel\ B}$ = 57, 56; N = 2). Kruskal-Wallis test was implemented (ns: p > 0.05, ****p ≤ 0.0001).

(C) Cells (5 × 10³) were seeded in 24-well plates and treated with doxorubicin at different concentrations for 24 h, after which cells were released in standard growth medium. Confluence was determined by Incucyte S3. Data were fitted with a logistic model, and growth rate was measured as the slope at the middle point. Results of two experiments were used for the analysis. Details of the analysis and statistical significance analysis are reported in STAR Methods. N = 2.

(D) Upper panels: we propose that the mitotic arrest induced by nocodazole results in mild caspase-3/7 activity and DNA damage (left). In cells that express higher levels of Triap1 (right), cytochrome *c* release from mitochondria is reduced, and cells experience less DNA damage and p21 activation. Lower panel: when cells undergo slippage, a few of them overexpress Triap1 (through an unknown process marked by "?"). These cells are selected and will resist more efficiently to the second treatment. See also Figure S7.

Regardless of the specific mechanism, we propose that, during the first recovery, dividing cells expressing such anti-apoptotic players are not detected in population studies since their signal is diluted by the 999/1,000 cells that do not resume proliferation. Their presence becomes evident at the end of recovery, when the dividing FC population is likely mostly formed of cells that originated from the 1/1,000 founders. These cells, when they undergo a second treatment, have already been selected, and thus recover faster (Figure 7D). Of note, we did not notice any further improvement after three cycles of nocodazole (not shown).

Mechanisms of Triap1 upregulation

A second source of uncertainty is the process underlying the upregulation of Triap1. On the one hand, it seems to be very stable, even genetically stable. FC and SC cells, as reiterated, for generations are desensitized to nocodazole. We hypothesized that it may be due to copy number variation driven by aneuploidy, but we did not detect any aneuploidy by performing NGS on the population of SC cells. This result only implies that there are not recurrent aneuploidies. However, this is what we looked for based on the fact that the higher levels of Triap1 were detected by mass spectrometry on the whole population, and not in single cells.

The fact that the behavior initially described in bulk populations was observed also in clones is not in favor of the presence of pre-existing mutations. There may rather be epigenetic processes underlying the phenotype. Triap1 mRNA is also targeted by several miRNAs that control its RNA abundance. As an example, downregulation of miRNA-320b has been shown to promote nasopharyngeal cancer progression by Triap1 overexpression.[28] Possibly, downregulation of some miRNAs may promote Triap1 mRNA stability and overexpression.

Limitations of the study

The fact that Triap1 overexpression was observed also in immortalized BJ cells, both in terms of anticipated recovery and higher Triap1 levels, suggests that the mechanism may be general. This conclusion comes with a word of caution. Both RPE1 and BJ cells used in this study are immortalized by hTERT expression. hTERT upregulation is instrumental for the escape from senescence induced by oncogenes overexpression,[33] and telomeric uncapping has been observed in response to prolonged mitotic arrest.[21] Hence, it is possible that our experimental system facilitates the escape from senescence by replacing uncapped telomeres, which activate the DNA damage response, via telomerase activity. However, the comet assay (Figure 2E) shows that the DNA damage response is not only induced by telomeric uncapping, but is due to actual DNA damage. Moreover, only ~1/1,000 cells managed to escape from the arrest while all of them overexpress hTERT, implying that other factors are required for the escape. Among them we propose Triap1 to play a key role.

STAR★METHODS

Detailed methods are provided in the online version of this paper and include the following:

- KEY RESOURCES TABLE
- RESOURCE AVAILABILITY
  - Lead contact
  - Materials availability
  - Data and code availability
- EXPERIMENTAL MODEL AND SUBJECT DETAILS
  - Cell culture
- METHOD DETAILS
  - Nocodazole cycles
  - SA β-galactosidase assay
  - Growth curves
  - Incucyte growth curves
  - Colony forming assay
  - MS analysis
  - DNA extraction
  - Time lapse imaging
  - Immunofluorescence
  - FACS cell cycle analysis
  - FACS intracell staining
  - Cell fractionation
  - Comet assay
  - Protein extraction and western blotting
  - RT qPCR
- QUANTIFICATION AND STATISTICAL ANALYSIS
  - Logistic growth analysis
  - MS database search
  - Analysis of proteomic dataset
  - Coverage analysis
  - Nuclear shape analysis and p53 quantification
  - Quantification of nuclear morphology
  - Quantification of cytochrome *c* localization
  - Quantification of gH2AX foci
  - Statistical analysis

AUTHOR CONTRIBUTIONS

M.P. designed and executed experiments, analyzed data, and contributed to writing the manuscript. E.C. and C.C. executed experiments. F.G. analyzed proteomic data and produced figures. P.B. analyzed data and produced Figure 7C. S.V. analyzed nuclear images. F.G. performed image analysis on cytochrome *c* and nuclear shape and produced figures. V.M. produced proteomics data. A.B. produced and analyzed proteomics data. L.L.F. designed experiments. T.L. designed and executed experiments. A.C. supervised the project, was responsible for funding, designed experiments, and wrote the manuscript. All co-authors gave their input and revised the manuscript.

DECLARATION OF INTERESTS

The authors declare no competing interests.

REFERENCES

1. Lara-Gonzalez, P., Pines, J., and Desai, A. (2021). Spindle assembly checkpoint activation and silencing at kinetochores. Semin. Cell Dev. Biol. *117*, 86–98. https://doi.org/10.1016/j.semcdb.2021.06.009.

2. Gascoigne, K.E., and Taylor, S.S. (2008). Cancer cells display profound intra- and interline variation following prolonged exposure to antimitotic drugs. Cancer Cell *14*, 111–122. https://doi.org/10.1016/j.ccr.2008.07.002.

3. Brito, D.A., and Rieder, C.L. (2006). Mitotic checkpoint slippage in humans occurs via cyclin B destruction in the presence of an active checkpoint. Curr. Biol. *16*, 1194–1200. https://doi.org/10.1016/j.cub.2006.04.043.

4. Rieder, C.L., and Maiato, H. (2004). Stuck in division or passing through: what happens when cells cannot satisfy the spindle assembly checkpoint. Dev. Cell *7*, 637–651. https://doi.org/10.1016/j.devcel.2004.09.002.

5. Topham, C., Tighe, A., Ly, P., Bennett, A., Sloss, O., Nelson, L., Ridgway, R.A., Huels, D., Littler, S., Schandl, C., et al. (2015). MYC is a major determinant of mitotic cell fate. Cancer Cell *28*, 129–140. https://doi.org/10.1016/j.ccell.2015.06.001.

6. Ganem, N.J., and Pellman, D. (2012). Linking abnormal mitosis to the acquisition of DNA damage. J. Cell Biol. *199*, 871–881. https://doi.org/10.1083/jcb.201210040.

7. Colin, D.J., Hain, K.O., Allan, L.A., and Clarke, P.R. (2015). Cellular responses to a prolonged delay in mitosis are determined by a DNA damage response controlled by Bcl-2 family proteins. Open Biol. *5*, 140156. https://doi.org/10.1098/rsob.140156.

8. Shi, J., and Mitchison, T.J. (2017). Cell death response to anti-mitotic drug treatment in cell culture, mouse tumor model and the clinic. Endocr. Relat. Cancer *24*, T83–T96. https://doi.org/10.1530/ERC-17-0003.

9. Allan, L.A., Skowyra, A., Rogers, K.I., Zeller, D., and Clarke, P.R. (2018). Atypical APC/C-dependent degradation of Mcl-1 provides an apoptotic timer during mitotic arrest. EMBO J. *37*, e96831. https://doi.org/10.15252/embj.201796831.

10. Harley, M.E., Allan, L.A., Sanderson, H.S., and Clarke, P.R. (2010). Phosphorylation of Mcl-1 by CDK1-cyclin B1 initiates its Cdc20-dependent destruction during mitotic arrest. EMBO J. *29*, 2407–2420. https://doi.org/10.1038/emboj.2010.112.

11. Shi, J., Zhou, Y., Huang, H.C., and Mitchison, T.J. (2011). Navitoclax (ABT-263) accelerates apoptosis during drug-induced mitotic arrest by antagonizing Bcl-xL. Cancer Res. *71*, 4518–4526. https://doi.org/10.1158/0008-5472.CAN-10-4336.

12. Budihardjo, I., Oliver, H., Lutter, M., Luo, X., and Wang, X. (1999). Biochemical pathways of caspase activation during apoptosis. Annu. Rev. Cell Dev. Biol. *15*, 269–290. https://doi.org/10.1146/annurev.cellbio.15.1.269.

13. Lanni, J.S., and Jacks, T. (1998). Characterization of the p53-dependent postmitotic checkpoint following spindle disruption. Mol. Cell Biol. *18*, 1055–1064. https://doi.org/10.1128/MCB.18.2.1055.

14. Dalton, W.B., Nandan, M.O., Moore, R.T., and Yang, V.W. (2007). Human cancer cells commonly acquire DNA damage during mitotic arrest. Cancer Res. *67*, 11487–11492. https://doi.org/10.1158/0008-5472.CAN-07-5162.

15. Quignon, F., Rozier, L., Lachages, A.M., Bieth, A., Simili, M., and Debatisse, M. (2007). Sustained mitotic block elicits DNA breaks: one-step alteration of ploidy and chromosome integrity in mammalian cells. Oncogene *26*, 165–172. https://doi.org/10.1038/sj.onc.1209787.

16. Uetake, Y., and Sluder, G. (2010). Prolonged prometaphase blocks daughter cell proliferation despite normal completion of mitosis. Curr. Biol. *20*, 1666–1671. https://doi.org/10.1016/j.cub.2010.08.018.

17. Fong, C.S., Mazo, G., Das, T., Goodman, J., Kim, M., O'Rourke, B.P., Izquierdo, D., and Tsou, M.-F.B. (2016). 53BP1 and USP28 mediate p53-dependent cell cycle arrest in response to centrosome loss and prolonged mitosis. Elife *5*, e16270. https://doi.org/10.7554/eLife.16270.

18. Lambrus, B.G., Daggubati, V., Uetake, Y., Scott, P.M., Clutario, K.M., Sluder, G., and Holland, A.J. (2016). A USP28–53BP1–p53–p21 signaling axis arrests growth after centrosome loss or prolonged mitosis. J. Cell Biol. *214*, 143–153. https://doi.org/10.1083/jcb.201604054.

19. Meitinger, F., Anzola, J.V., Kaulich, M., Richardson, A., Stender, J.D., Benner, C., Glass, C.K., Dowdy, S.F., Desai, A., Shiau, A.K., and Oegema, K. (2016). 53BP1 and USP28 mediate p53 activation and G1 arrest after centrosome loss or extended mitotic duration. J. Cell Biol. *214*, 155–166. https://doi.org/10.1083/jcb.201604081.

20. Orth, J.D., Loewer, A., Lahav, G., and Mitchison, T.J. (2012). Prolonged mitotic arrest triggers partial activation of apoptosis, resulting in DNA damage and p53 induction. Mol. Biol. Cell *23*, 567–576. https://doi.org/10.1091/mbc.E11-09-0781.

21. Hayashi, M.T., Cesare, A.J., Fitzpatrick, J.A.J., Lazzerini-Denchi, E., and Karlseder, J. (2012). A telomere-dependent DNA damage checkpoint induced by prolonged mitotic arrest. Nat. Struct. Mol. Biol. *19*, 387–394. https://doi.org/10.1038/nsmb.2245.

22. Cimini, D., Howell, B., Maddox, P., Khodjakov, A., Degrassi, F., and Salmon, E.D. (2001). Merotelic kinetochore orientation is a major mechanism of aneuploidy in mitotic mammalian tissue cells. J. Cell Biol. *153*, 517–527. https://doi.org/10.1083/jcb.153.3.517.

23. Crasta, K., Ganem, N.J., Dagher, R., Lantermann, A.B., Ivanova, E.V., Pan, Y., Nezi, L., Protopopov, A., Chowdhury, D., and Pellman, D. (2012). DNA breaks and chromosome pulverization from errors in mitosis. Nature *482*, 53–58. https://doi.org/10.1038/nature10802.

24. Ichim, G., Lopez, J., Ahmed, S.U., Muthalagu, N., Giampazolias, E., Delgado, M.E., Haller, M., Riley, J.S., Mason, S.M., Athineos, D., et al. (2015). Limited mitochondrial permeabilization causes DNA damage and genomic instability in the absence of cell death. Mol. Cell *57*, 860–872. https://doi.org/10.1016/j.molcel.2015.01.018.

25. Park, W.R., and Nakamura, Y. (2005). p53CSV, a novel p53-inducible gene involved in the p53-dependent cell-survival pathway. Cancer Res. *65*, 1197–1206. https://doi.org/10.1158/0008-5472.CAN-04-3339.

26. Andrysik, Z., Kim, J., Tan, A.C., and Espinosa, J.M. (2013). A genetic screen identifies TCF3/E2A and TRIAP1 as pathway-specific regulators of the cellular response to p53 activation. Cell Rep. *3*, 1346–1354. https://doi.org/10.1016/j.celrep.2013.04.014.

27. Potting, C., Tatsuta, T., König, T., Haag, M., Wai, T., Aaltonen, M.J., and Langer, T. (2013). TRIAP1/PRELI complexes prevent apoptosis by mediating intramitochondrial transport of phosphatidic acid. Cell Metabol. *18*, 287–295. https://doi.org/10.1016/j.cmet.2013.07.008.

28. Li, Y., Tang, X., He, Q., Yang, X., Ren, X., Wen, X., Zhang, J., Wang, Y., Liu, N., and Ma, J. (2016). Overexpression of mitochondria mediator gene TRIAP1 by miR-320b loss is associated with progression in nasopharyngeal carcinoma. PLoS Genet. *12*, e1006183. https://doi.org/10.1371/journal.pgen.1006183.

29. Adams, C., Cazzanelli, G., Rasul, S., Hitchinson, B., Hu, Y., Coombes, R.C., Raguz, S., and Yagüe, E. (2015). Apoptosis inhibitor TRIAP1 is a novel effector of drug resistance. Oncol. Rep. *34*, 415–422. https://doi.org/10.3892/or.2015.3988.

30. Uetake, Y., and Sluder, G. (2018). Activation of the apoptotic pathway during prolonged prometaphase blocks daughter cell proliferation. Mol. Biol. Cell *29*, 2632–2643. https://doi.org/10.1091/mbc.E18-01-0026.

31. Jakhar, R., Luijten, M.N.H., Wong, A.X.F., Cheng, B., Guo, K., Neo, S.P., Au, B., Kulkarni, M., Lim, K.J., Maimaiti, J., et al. (2018). Autophagy governs protumorigenic effects of mitotic slippage–induced senescence. Mol. Cancer Res. *16*, 1625–1640. https://doi.org/10.1158/1541-7786.MCR-18-0024.

32. Burigotto, M., Mattivi, A., Migliorati, D., Magnani, G., Valentini, C., Roccuzzo, M., Offterdinger, M., Pizzato, M., Schmidt, A., Villunger, A., et al. (2021). Centriolar distal appendages activate the centrosome-PIDDosome-p53 signalling axis via ANKRD26. EMBO J. *40*, e104844. https://doi.org/10.15252/embj.2020104844.

33. Patel, P.L., Suram, A., Mirani, N., Bischof, O., and Herbig, U. (2016). Derepression of hTERT gene expression promotes escape from oncogene-induced cellular senescence. Proc. Natl. Acad. Sci. USA *113*, E5024–E5033. https://doi.org/10.1073/pnas.1602379113.

34. Rappsilber, J., Ishihama, Y., and Mann, M. (2003). Stop and go extraction tips for matrix-assisted laser desorption/ionization, nanoelectrospray, and LC/MS sample pretreatment in proteomics. Anal. Chem. *75*, 663–670. https://doi.org/10.1021/ac026117i.

35. Matafora, V., Corno, A., Ciliberto, A., and Bachi, A. (2017). Missing value monitoring enhances the robustness in proteomics quantitation. J. Proteome Res. *16*, 1719–1727. https://doi.org/10.1021/acs.jproteome.6b01056.

36. Cox, J., and Mann, M. (2008). MaxQuant enables high peptide identification rates, individualized p.p.b.-range mass accuracies and proteome-wide protein quantification. Nat. Biotechnol. *26*, 1367–1372. https://doi.org/10.1038/nbt.1511.

37. Cox, J., Neuhauser, N., Michalski, A., Scheltema, R.A., Olsen, J.V., and Mann, M. (2011). Andromeda: a peptide search engine integrated into the MaxQuant environment. J. Proteome Res. *10*, 1794–1805. https://doi.org/10.1021/pr101065j.

38. Zhang, X., Smits, A.H., Van Tilburg, G.B., Ovaa, H., Huber, W., and Vermeulen, M. (2018). Proteome-wide identification of ubiquitin interactions using UbIA-MS. Nat. Protoc. *13*, 530–550. https://doi.org/10.1038/nprot.2017.147.

39. Leek JT, J.W., Parker, H.S., Fertig, E.J., Jaffe, A.E., Zhang, Y., Storey, J.D., and Torres, L.C. (2022). sva: Surrogate Variable Analysis. R package version 3.44.0.

40. Ritchie, M.E., Phipson, B., Wu, D., Hu, Y., Law, C.W., Shi, W., and Smyth, G.K. (2015). Limma powers differential expression analyses for RNA-sequencing and microarray studies. Nucleic Acids Res. *43*, e47. https://doi.org/10.1093/nar/gkv007.

41. Alexa A, R.J. (2022). Limma Powers Differential Expression Analyses for RNA-Sequencing and Microarray Studies. topGO: Enrichment Analysis for Gene Ontology. *R package version 2.48.0*.

42. Zhou, Y., Zhou, B., Pache, L., Chang, M., Khodabakhshi, A.H., Tanaseichuk, O., Benner, C., and Chanda, S.K. (2019). Metascape provides a biol-ogist-oriented resource for the analysis of systems-level datasets. Nat. Commun. *10*, 1523. https://doi.org/10.1038/s41467-019-09234-6.

43. Pomaznoy, M., Ha, B., and Peters, B. (2018). GOnet: a tool for interactive Gene Ontology analysis. BMC Bioinf. *19*, 470. https://doi.org/10.1186/s12859-018-2533-3.

44. Shannon, P., Markiel, A., Ozier, O., Baliga, N.S., Wang, J.T., Ramage, D., Amin, N., Schwikowski, B., and Ideker, T. (2003). Cytoscape: a software environment for integrated models of biomolecular interaction networks. Genome Res. *13*, 2498–2504. https://doi.org/10.1101/gr.1239303.

45. Bolger, A.M., Lohse, M., and Usadel, B. (2014). Trimmomatic: a flexible trimmer for Illumina sequence data. Bioinformatics *30*, 2114–2120. https://doi.org/10.1093/bioinformatics/btu170.

46. Li, H., and Durbin, R. (2010). Fast and accurate long-read alignment with Burrows–Wheeler transform. Bioinformatics *26*, 589–595. https://doi.org/10.1093/bioinformatics/btp698.

47. Faust, G.G., and Hall, I.M. (2014). SAMBLASTER: fast duplicate marking and structural variant read extraction. Bioinformatics *30*, 2503–2505. https://doi.org/10.1093/bioinformatics/btu314.

48. Li, H., Handsaker, B., Wysoker, A., Fennell, T., Ruan, J., Homer, N., Marth, G., Abecasis, G., and Durbin, R.; 1000 Genome Project Data Processing Subgroup (2009). The sequence alignment/map format and SAMtools. Bioinformatics *25*, 2078–2079. https://doi.org/10.1093/bioinformatics/btp352.

49. Danecek, P., Bonfield, J.K., Liddle, J., Marshall, J., Ohan, V., Pollard, M.O., Whitwham, A., Keane, T., McCarthy, S.A., Davies, R.M., and Li, H. (2021). Twelve years of SAMtools and BCFtools. GigaScience *10*, giab008. https://doi.org/10.1093/gigascience/giab008.

STAR★METHODS

KEY RESOURCES TABLE

REAGENT or RESOURCE	SOURCE	IDENTIFIER
Antibodies		
Anti γH2AX	Millipore	05636; RRID:AB_2755003
Anti Mad1	Abcam	ab175245
Anti human Centromere	Antibodies Incorporated	15-234; RRID:AB_2687472
Anti p53	SantaCruz	Sc-126; RRID:AB_628082
Anti Cytochrome C	BD phamigen	556432; RRID:AB_396416
Anti Cytochrome C	MitoScience	MSA06; RRID:AB_478285
Anti p21	Cell Signaling	2946; RRID:AB_2260325
Anti Triap1	Invitrogen	PA576211
Anti Vinculin	Sigma	V9131; RRID:AB_477629
Anti GAPDH	Cell Signaling	Sc32233
Anti ATP5A	Abcam	AB14748; RRID:AB_301447
Anti Cleaved Caspase 3	Cell Siganaling	9661; RRID:AB_2341188
Anti mouse Alexa 488	ThermoFisher	A-11001; RRID:AB_2534069
Anti mouse Alexa 647	ThermoFisher	A32728; RRID:AB_2633277
Anti Rabbit Alexa 488	ThermoFisher	A-11001; RRID:AB_2534069
Anti Rabbit Alexa 647	ThermoFisher	A32733; RRID:AB_2633282
Anti mouse HRP	ThermoFisher	31430; RRID:AB_228307
Anti rabbit HRP	ThermoFisher	32260; RRID:AB_2549733
Chemicals, peptides, and recombinant proteins		
Nocodazole	SigmaAldrich	M1404
Thymidine	SigmaAldrich	T1895
Centrinone	biotechne	5687/10
H_2O_2	SigmaAldrich	H1009
Dulbecco's Modified Eagle Medium/F-12	ThermoFisher Scientific	10565018
Fetal Bovine Serum	biotechne	S11150
DMEM	Euroclone	ECB7501L
M199	ThermoFisher Scientific	41150
Critical commercial assays		
Cell Fractionation Kit - Standard	Abcam	ab109719
Cell Titer glo 2.0	Promega	G9241
Trevigen Bio-techne comet assay kit	Bio-techne	4250-050-K
SYBR Green master mix	Roche	04887352001
Maxwell® RSC simplyRNA Tissue Kit	Promega	AS1340
SuperScript VILO cDNA Synthesis Kit	Thermofisher	11754050
Deposited data		
Mass Spectrometry data	ProteomeXchange Consortium via the PRIDE	PXD037143
Experimental models: Cell lines		
hTERT-RPE1	ATCC	CRL-4000
hTERT-RPE1 EmptyVector	This study	NA
hTERT-RPE1 Triap1 OE	This study	NA
hTERT-RPE1 FirstCycle shScramble	This Study	NA
hTERT-RPE1 FirstCycle shTriap1	This study	NA
hTERT-RPE1 p53KO	Burigotto et al., EMBO J, 2021[32]	NA

REAGENT or RESOURCE	SOURCE	IDENTIFIER
Continued		
hTERT-RPE1 53BP1KO	Burigotto et al., EMBO J, 2021[32]	NA
BJ-hTERT (BJ-5ta)	ATCC	CRL-4001
Oligonucleotides		
GAPDH For (GCACCGTCAAGGCTGAGAAC)	This study	NA
GAPDH Rev (TGGTGAAGACGCCAGTGGA)	This study	NA
Triap1 For (AGGATTTCGCAAGTCCAGAA)	This study	NA
Triap1 Rev (GCTGATTCCACCCAAGTAT)	This study	NA
Recombinant DNA		
pLV-EGFP:T2A:Puro-U6-shScramble	VectorBuilder	VB010000-0009mxc
pLV-EGFP:T2A:Puro-U6- shTriap1	VectorBuilder	VB210215-1098ntm
plenti-CMV-GFP-Puro	Amsgood	477370610395
plenti-CMV-Triap1-GFP-Puro	Amsgood	LV590
Software and algorithms		
FlowJo	Becton, Dickinson and Company	https://www.flowjo.com
Fiji	NIH	https://imagej.net/software/fiji/
R (version 4.0.3)	R-project	https://www.r-project.org/
MATLAB	MathWorks	https://it.mathworks.com/

RESOURCE AVAILABILITY

Lead contact
Further information and requests for resources and reagents should be directed to and will be fulfilled by the Lead Contact, Andrea Ciliberto (andrea.ciliberto@ifom.eu).

Materials availability
Materials generated in this study (e.g. cell lines) are available upon MTA completion on request from the lead contact.

Data and code availability
- Mass spectrometry data have been deposited to the ProteomeXchange Consortium via the PRIDE partner repository with the dataset identifier: PXD037143.
- Raw data are available from the lead contact upon request. All original codes generated in this study are available in supplemental information.
- Any additional information required to reanalyze the data reported in this paper is available from the lead contact upon request.

EXPERIMENTAL MODEL AND SUBJECT DETAILS

Cell culture
All experiments were performed on hTERT-RPE1 cells except for experiments in Figures 4E and S1E which were performed with hTERT-BJ cells.

Human retinal epithelial hTERT-RPE1 cells were grown in Dulbecco's Modified Eagle Medium/F-12 (1:1) (DMEM/F12, Gibco) supplemented with 10% Fetal Bovine Serum (FBS Life-technologies). hTERT-BJ (BJ-5ta) cells were grown in DMEM (Euroclone) supplemented with M199 1x (1:4) (Life Techologies), 10%FBS and 2mM L-Glutamine.

hTERT-RPE1 overexpressing Triap1 and Empty Vector, as well as shScramble/Triap1 were generated by lentiviral infection. 3rd generations vectors for Triap1 overexpression and Empty Vector control were purchased from Amsgood (plenti-CMV-GFP-Puro). Triap1 Vector contained the gene CDS (BC002638) under a CMV promoter, Puromycin resistance cassette and GFP reporter cassette. shScramble (5′-CCTAAGGTTAAGTCGCCCTCG-3′) and shTriap1 (5′ AGAGATTCCTATTGAAGGACTGGAGTTCA-3′[29]) 3rd generation lentiviral vectors (pLV-EGFP:T2A:Puro-U6) were purchased by VectorBuilder.

hTERT-RPE1 p53KO and 53BP1KO cell lines were gifted by Dr. Luca Fava (UniTrento, Italy).[32]

Thymidine (T1895 Sigma-Aldrich) and Nocodazole (M1404 Sigma-Aldrich) were used respectively 2.5mM and 100nM. Doxorubicin was gifted by Dr. Claudio Vernieri (IFOM ETS, INT).

METHOD DETAILS

Nocodazole cycles

Nocodazole treatment was implemented as designed in Figures 1A and 1B: hTERT-RPE1 cells were synchronized in thymidine 2.5 mM for 24h and released in nocodazole 100nM for 16h. Mitotic arrested cells were collected by shake off and plated in nocodazole for 56h, then released and seeded for subsequent analysis. This procedure was implemented once for First Cycle cells and twice for Second Cycle cells. The second cycle of treatment was done on First Cycle cells after 2 weeks from the first treatment.

SA β-galactosidase assay

Cells were treated with nocodazole as described above. After the shake off, 3×10^5 cells were plated in nocodazole onto glass coverslips in 6 well plates. Cells were then fixed and stained after 56h (Recovery Day0). Cyclin RPE1 cells were plated onto coverslips and fixed when the confluence approached to 70–80%. Coverslips were transferred in a 12 well plate and fixed with PFA 4% for 10 min RT. Then coverslips were washed 3 times with PBS 1X and incubated overnight with 2 mL of β-Galactosidase staining mix. The latter was composed by: Sodium Phosphate buffer 0.5M pH 6.0, Potassium Hexacyanoferrate 2mM, Potassium Ferricyanide 2mM, NaCl 2.4M, $MgCl_2$ 0.8M and X-Gal 1 mg/ml. Then coverslips were washed 3 times with PBS 1X and fixed in PFA 4X for 10 min at RT. Afterward, coverslips were washed 3 times in PBS 1X and cells were permeabilized with Triton X-100 0.2% - PBS for 10 min at RT. Coverslips were incubated with DAPI for 10 min RT and mounted with Mowiol. Images were acquired with a widefield microscope equipped with an RGB camera.

Growth curves

Cells were treated with nocodazole as described in the previous section. After treatment (Recovery Day0) cells were released and 2×10^4 cells were plated in triplicate in 6 well plates. One 6 well for each time point was prepared and medium was replaced twice a week. Cells were counted every 2/3 days till the confluence of the 6 well (1×10^6 cells, ATCC) using Scepter 3.0 with 60μm sensors.

Incucyte growth curves

After treatment (Recovery Day0) cells were released and 4×10^3 cells were plated in 24 well in duplicate. Cells were imaged every 6h by using Incucyte S3 and 36 images were acquired for each well. Media was replaced twice a week. Confluence was determined by Incucyte Software: it corresponds to the total imaged area divided by the area occupied by cells. The mean confluence value and the SEM of the pooled replicates and images were plotted. To estimate the slope as proxy of growth rate, a logistic model was fitted using R studio software.

Colony forming assay

Cells were treated with nocodazole as described above. After treatment (Recovery Day0) cells were released and plated in 6-well at different dilutions (5000, 2500, 1000, 500, 250, 100 cells/well). At the specified time points cells were rinsed with PBS and stained for few minutes with Crystal Violet (Sigma-Aldrich) then washed with deionized water. 6-well plates were then scanned with Epson perfection V370 photo scanner.

MS analysis

Proteins were extracted by 8M Urea treatment and sonication (Bioruptor) and quantified with Bradford (Biorad) from exponentially growing RPE1, First Cycle and Second Cycle cells.

For MS analysis, 50 μg of protein extract was added to 50 μL of 8M urea in 0.1 M Tris/HCl, pH 8.5 (UA) and the samples were transferred to YM-30 micron filters (Cat No. MRCF0R030, Millipore) and centrifuged at 14,000×g for 15 min. Then, cysteines reduction and alkylation was performed adding 200 μL of TCEP (Thermo scientific) 10 mM and 2-Chloroacetamide (Sigma-Aldrich) 40 mM in Urea 8 M Tris100 mM pH 8 for 30 min at room temperature. Filters were washed twice with 100 μL of 8M UA followed by two washes with 100 μL of 40 mM NH4HCO3. Finally, 2 μg of trypsin were added in 95 μL of 40 mM NH4HCO3. Samples were incubated overnight at 37°C, then 1μg of trypsin was added for further 3h of incubation. Released peptides were collected by centrifugation. The resulting peptides were purified on a C18 StageTip (Proxeon Biosystems, Denmark).[34] 1 μg of digested sample was injected onto a quadrupole Orbitrap Q-exactive HF mass spectrometer (Thermo Scientific). Peptides separation was achieved on a linear gradient from 95% solvent A (2% ACN, 0.1% formic acid) to 55% solvent B (80% acetonitrile, 0.1% formic acid) over 117 min and from 55% to 100% solvent B over 3 min at a constant flow rate of 0.25 μL/min on UHPLC Easy-nLC 1000 (Thermo Scientific) where the LC system was connected to a 23-cm fused-silica emitter of 75 μm inner diameter (New Objective, Inc. Woburn, MA, USA), packed in-house with ReproSil-Pur C18-AQ 1.9 μm beads (Dr Maisch Gmbh, Ammerbuch, Germany) using a high-pressure bomb loader (Proxeon, Odense, Denmark).

The mass spectrometer was operated in DDA mode as described previously.[35] Missing value monitoring enhances the robustness in proteomics quantitation. Dynamic exclusion was enabled (exclusion duration = 15 s), MS1 resolution = 70,000, MS1 automatic gain control target = 3×10^6, MS1 maximum fill time = 60 ms, MS2 resolution = 17,500, MS2 automatic gain control target = 1×10^5, MS2 maximum fill time = 60 ms, and MS2 normalized collision energy = 25. For each cycle, one full MS1 scan range = 300–1650 m/z, was followed by 12 MS2 scans using an isolation window size of 2.0 m/z.

DNA extraction

Genomic DNA was extracted from exponentially growing RPE1, First Cycle cells using Qiagen genomic extraction Kit according to guidelines. NGS sequencing was performed by Biodiversa srl (Treviso, Italy).

Time lapse imaging

$2,5/3,5 \times 10^4$ cells were plated onto IBIDI® slides and synchronized in thymidine. After 24h cells were released in DMEM-F12 medium (without phenol) containing nocodazole. The medium surface was coated with sterile mineral oil to avoid evaporation and cells dehydration. Images were acquired using DeltaVision Elite (GE-Healthcare) CoolSNAP HQ CCD camera using a 60× immersion objective (Olimpus). 4 z stacks (4 μm) were acquired for 40h using 32% of POL intensity exposed for 0.1 s. Temperature of 37°C and 5%CO$_2$ were maintained with Okolab incubator. Images were then analyzed using ImageJ software. The time in mitosis is considered from the Nuclear Envelop Break Down (NEBD) to cell re-adhesion.

Immunofluorescence

For IF analysis $1/2 \times 10^5$ pre-synchronized S phase cells were plated in nocodazole onto coverslips in a 6-well plate and permeabilized in 0.5% Triton X-100-PHEM (Sigma) for 5 min at room temperature. To maintain cell morphology PFA 4% was dissolved in PHEM buffer (Pipes 60 mM, Hepes 25mM pH 6, EGTA 10mM pH 8, MgSO4 4mM, milli-Q H2O). Following permeabilization few drops of PFA 4%-PHEM were added to cells without removing Triton X-100-PHEM for 2 min to gradually fix them. Then coverslips were incubated for 20 min in PFA 4%-PHEM alone. For γH2AX foci and Cytochrome *c* analysis, cells were fixed in PFA4%-PBS for 10 min and permeabilized with 0.5% Triton X-100-PBS. Then coverslips were washed in PBS three times for 5 min and treated with glycine 25 mM to quench unreacted aldehydes. Then, samples were blocked with PBS-Tween 0,1%-BSA 3% (PBS-T-BSA3%) for at least 30 min.

For coverslips staining primary antibodies were diluted 1:500 in PBS-T-BSA3% and incubated for 1 h at room temperature. Anti γH2AX, anti p53 and anti-Cytochrome C were purchased respectively from Millipore (JBW301), Santa Cruz (DO-1) and BD pharmigen (6H2.B4). Samples were washed three times in PBS-T and once in PBS. Secondary antibody: Anti-mouse Alexa 488/647 (Life-technologies) was diluted 1:400 in PBS-T-BSA3% together with DAPI (Sigma, 1:1000) and Phalloidin TRICT (1:50) (life-technologies). Secondary antibody was incubated for 45 min in the dark at room temperature. Coverslips were then mounted with Mowiol or glycerol (Calbiochem) on microscopy slides. Images were acquired by using DeltaVision Elite (GE-Healthcare) CoolSNAP HQ CCD camera with a 100X, 40X or 20× objective (Olimpus). Confocal images were acquired with Leica SP8-STED with a 40× objective. ∼ 40 confocal planes distant 0.50 μm were acquired for each image. Images were analyzed with ImageJ software.

FACS cell cycle analysis

Cells were incubated with 33 μM BrdU for 20 min, collected and centrifuged at 225G for 10 min. The pellet was re-suspended in 750μL of PBS1X and fixed by adding 2250μL of ice-cold (−20°C) pure ethanol dropwise while vortexing. Samples were washed once in 1% BSA/PBS and re-suspended in 1 mL of 2N HCl and incubated for 25 min at room temperature allowing DNA denaturation. Then 3mL of 0.1M Sodium Borate (pH 8,5) was added to neutralize the acidic pH of the HCl solution and samples were incubated at room temperature for 2 min, centrifuged and washed twice in 1%BSA/PBS. Samples were then transferred in Eppendorf tube and centrifuged at 805 G for 5 min. Pellets were re-suspended in 100μL of pure anti-BrdU antibody (life-technologies) diluted 1:5 in 1%BSA/PBS and incubated for 1 h at room temperature in the dark. Samples were washed with 1%BSA/PBS and re-suspended in 100μL of anti-mouse FITC (life-technologies) diluted 1:50 in 1%BSA/PBS for 1 h at room temperature in the dark. After washing once with 1%BSA/PBS pellets were re-suspended in 1 mL of Propidium Iodate (PI) (2.5 μg/mL) and RNase (250 μg/mL) (RibonucleaseA from bovine pancreas, Sigma) and incubated overnight at 4°C. Acquisition was made with FACScalibur and data analysis was performed with FlowJo software.

FACS intracell staining

For each cell line, 10^6 exponentially growing cells were fixed in 1%PFA-PBS for 20′, resuspended PBS and permeabilized for 5′ with Triton X-100 0.25% in PBS. Then they were blocked for 45 min in 5%BSA-PBS, stained 2h at RT with anti-Triap1 (Invitrogen PA5-76211), anti-p21 (Cell Signaling DCS60) or anti-cleaved Asp175 Caspase3 (Cell Signaling 9661) 1:100. After washing once in PBS-tween 0.2%, samples were incubated for 1h with secondary antibody 1:400 (anti-rabbit 647, life-technologies), washed with BSA1%/PBS, and resuspended in PBS. Samples were acquired using Attune (Thermo Scientific): 647 fluorescence were acquired with RL1 lasers at Attune (Themofisher). fcs files were analyzed using a customized R script.

Cell fractionation

Mitotic arrested cells were collected by shake off after 16h nocodazole treatment on pre-synchronized S phase cells (24h of 2.5mM Thymidine block). To induce a complete MOMP, cells were treated with H$_2$O$_2$ 0.5mM for 16h. Untreated cells were collected from an exponentially growing population.

Cytosolic (C) and Mitochondrial (M) fractions were extracted with Cell Fractionation Kit - Standard (ab109719) according to guidelines. Samples were loaded on precast gel and analyzed by Western Blot.

Comet assay

Mitotic arrested cells were collected by shake off after 16h of nocodazole treatment on pre-synchronized S phase cells (24h of 2.5mM Thymidine block). Comet assay was performed using Trevigen Bio-techne kit according to guidelines. As control samples, cells were treated with H_2O_2 0.5mM for 20 min at 4C. Untreated cells were collected from an exponentially growing population. Comet slides were stained with Syber Gold (Invitrogen) and images were acquired at DeltaVision Elite (GE-Healthcare) CoolSNAP HQ CCD camera with a 10× objective (Olimpus). Comets analysis was performed using OpenComet Fiji plugin.

Protein extraction and western blotting

Cells were detached from a sub-confluent flask (70–80%) using 0.05% Trypsin, washed once in DPBS and re-suspended in 200 μL of RIPA buffer (150 mM sodium chloride; 50 mM Tris pH 8.0; 1.0% NP-40; antiproteoltic agents (Calbiochem); DTT 1mM (Sigma-Aldrich)). Samples were incubated on ice for 15 min, transferred in an Eppendorf tube and then incubated on ice for other 15 min. After centrifugation at 4 °C at 17,000 G for 20 min, samples were loaded on a Biorad precast gel and transferred using TURBO blot apparatus (Biorad) on Nitrocellulose membrane. Membranes were blocked for 1h at RT in 5% Milk diluted in TBS +2%Tween (TBS-T). Primary antibodies were diluted in 5%Milk TBS-T and incubated overnight at 4°C. anti-p53 (DO-1 Santa Cruz), anti-p21 (cell signaling 2946), anti-Vinculin (Sigma), anti-Cytochrome C (Mitosciences MSA06), anti-Gapdh (Cytosolic marker sc32233 SantaCruz) and anti-Atp5A (Mitochondrial marker 15H4C4 ab14748 abcam) antibodies were diluted 1:1000. Membranes were washed three times (10 min each) in TBS-T and incubated 1.5h at RT with secondary antibody (Anti-mouse HRP, life-technologies) diluted 1:10,000 in 5%Milk TBS-T, washed three times (15 min each) in TBS-T, and developed using Dura ECL (thermofisher-scientific).

RT qPCR

Total RNA from cultured cells was extracted with Maxwell® RSC simplyRNA Tissue Kit with the Maxwell® RSC Instrument (Promega) using the "simply RNA tissue method", according to manufacturer instructions. Briefly, cells were centrifuged at low speed and pellet was dissolved in 1-Thioglicerol/Homogenization Solution and loaded in the cartridge. 150 ng of RNA were retro-transcribed using the SuperScript VILO cDNA Synthesis Kit (Thermofisher, Cat number 11754050). RT-qPCR experiments were performed on a Roche LightCycler 96 and the reactions were prepared using SYBR Green master mix (Roche). TRIAP1 was amplified using the following oligos: 5′-AGGATTTCGCAAGTCCAGAA-3′ and 5′-GCTGATTCCACCCAAGTAT-3′. GAPDH was used as housekeeping and amplified using the following oligos: 5′- GCACCGTCAAGGCTGAGAAC-3′ and 5′-TGGTGAAGACGCCAGTGGA-3′.

QUANTIFICATION AND STATISTICAL ANALYSIS

Logistic growth analysis

We fitted the confluence curves using a logistic-growth model based on the following equation:

$$confluence = \frac{100}{1 + e^{(middle - t) * slope}}$$

where t is the time in hours. Curves are fitted to full confluence, or to the end of the experiment if they do not reach full confluence.

To compare Untreated and Adapted cells, we fitted the data from both populations with a single model in which we included a dummy variable D: D is 1 for Untreated cells and 0 otherwise. By using D, we decomposed both middle and slope as follows:

$$confluence = \frac{100}{1 + e^{(middle_1 + middle_2 * D) - t) * (slope_1 + slope_2 * D)}}$$

The p value presented in Figure 7C is the p value of the estimate of slope2, which measures the difference in growth rate of the two cell groups.

MS database search

Raw MS files were processed with MaxQuant software (1.5.2.8).[36] MaxQuant enables high peptide identification rates, identifies ppb-range mass accuracies and proteome-wide protein quantification making use of the Andromeda search engine.[37] MS/MS peak lists were searched against the UniProtKB Human complete proteome database (uniprot_cp_human_2015_03) in which trypsin specificity was used with up to two missed cleavages allowed. Searches were performed selecting alkylation of cysteine by carbamidomethylation as fixed modification, oxidation of methionine, N-terminal acetylation and N-Deamination as variable modifications. Mass tolerance was set to 5 ppm and 10 ppm for parent and fragment ions, respectively. A reverse decoy database was generated within Andromeda and the False Discovery Rate (FDR) was set to <0.01 for peptide spectrum matches (PSMs). For identification, at least two peptides identifications per protein were required, of which at least one peptide had to be unique to the protein group.

Analysis of proteomic dataset

Data analysis based on LFQ intensities was performed using the R Bioconductor Package "DEP".[38] The data were background-corrected and normalized by variance stabilizing transformation (vsn). Only proteins that had at least one non-missing value for each

relevant condition were kept in the dataset. The remaining missing values were imputed using the quantile regression-based left-censored function ("QRILC"). All pre-processing steps were performed including two additional conditions that were not used in the subsequent analysis. PCA revealed batch effects for experiments performed on different days. Batch correction was performed using the R Bioconductor package "sva".[39] Differential enrichment analysis was performed on batch-uncorrected expression values with the R Bioconductor package "limma",[40] applying linear models with a moderated t test statistic adding batch group as an additional co-variate while adjusting for possible correlation of technical replicates.

We performed a consistency check for MS data, and confirmed by PCA analysis after batch correction that different replicates of the same condition cluster together (Figure S4A).

Gene ontology analysis in Table S1 was carried out with the R Bioconductor package "topGO",[41] using Fisher's exact test for proteins with adjusted p value <0.05. Protein involved in apoptosis in Figure 4B were determined by metascape[42] (https://metascape. org) implementing a GO analysis on up- or down-regulated proteins (GO:1902253: regulation of intrinsic apoptotic signaling pathway by p53 class mediator, GO:1902229 regulation of intrinsic apoptotic signaling pathway in response to DNA damage, GO:2001242 regulation of intrinsic apoptotic signaling pathway, GO:0097193 intrinsic apoptotic signaling pathway, GO:2001243 negative regulation of intrinsic apoptotic signaling pathway, GO:0008630 intrinsic apoptotic signaling pathway in response to DNA damage). The graph in Figure 4C was created using GOnet[43] and Cytoscape.[44]

Coverage analysis

The FASTA files were trimmed using trimmomatic v0.36[45] and aligned to the reference sequence (GRCh38) using Burrows-Wheeler Aligner (BWA) v0.7.17.[46] Afterward, duplicates were removed using samblaster v0.1.24[47] and sorted using samtools v1.9.[48,49]

Information about depth of coverage was extracted from bam files using a custom script written in python that makes use of the "depth" function contained in the samtools package. Chromosomes were partitioned into bins of 10,000 bp, and the bin-wise median was used for further analysis.

Nuclear shape analysis and p53 quantification

Nuclear shape analysis and p53 quantification were made using ImageJ software: nuclei were detected thresholding the maximum projection of the DAPI channel to create a ROI of each single nucleus. ROI shapes were used to asses nuclear morphology. The same ROIs were used to quantify p53 using its average projection.

Quantification of nuclear morphology

The resolution of the acquired images was not constant across different experiments (the effective pixel size p varying between 0.321 mm and 0.649 mm). To mitigate the potential biases in the estimation of the morphological parameters related to the roughness of the nuclear boundaries, we adopted the following procedure. For each ROI (identified as described previously): i) we generated the corresponding binary image B_1 ($B_1 = 1$ for all pixels within the ROI, $B_1 = 0$ otherwise), ii) we convolved B_1 with a smoothing Gaussian filter G_σ of width $\sigma = c/p$, with $c = 0.3 \, \mu m$, and iii) we obtained a corrected binary image B_2 by applying a threshold to the result of the convolution operation. Formally:

$$B_2 = \Theta(B_2 \star G_\sigma - 0.5)$$

where Θ is the Heaviside function, and the symbol $\star$ indicates the convolution operation.

Once obtained the corrected binary image B_2, we measured the perimeter P of the corresponding ROI, the area A, the convex area A_c (i.e. the area of the convex hull of the region), the length of the major axis M, and of the minor axis m of the ellipse that has the same principal second central moments as the region.

If a ROI was composed by multiple separated components (i.e. if the corresponding nucleus is fragmented) the above parameters were evaluated for each fragment.

For each non-fragmented nucleus, we estimated the circularity as $C = 4\pi A/P^2$, the solidity as $S = A/A_c$ and the aspect ratio as $a_R = M/m$.

The circularity index C captures any deviation of the ROI from a circular shape. $C = 1$ for a perfect circle, while $C < 1$ if the region has rough boundaries and/or an elongated shape. The solidity index S enables identifying the presence of concave portions in the ROI boundary. $S = 1$ if the region is convex, while in the presence of any indentations, $S < 1$. Unlike the previously considered indexes, the aspect ratio a_R is not very sensitive to the details of the ROI boundary, as it captures its overall degree of anisotropy. If the ROI is circularly symmetric (or, more generally, if its principal second central moments are equal) $a_r = 1$, while $a_r > 1$ if the ROI has an elongated shape.

All the above-described calculations have been implemented in a custom MATLAB code (Nuclear_Shape_Quantification.m included in supplemental information).

Quantification of cytochrome c localization

For each field of view (FOV), a z-stack $I_z(\boldsymbol{x})$ was collected as described in section 'immunofluorescence'. Each individual cell within the FOV was manually segmented (Figure S7D panel a), identifying the corresponding region of interest (ROI). For each layer z, we evaluated the mean intensity $\langle I_z(\boldsymbol{x})\rangle_{ROI}$ on the Cytochrome C channel within the ROI, and we calculated a variance map defined as

$V_z(\mathbf{x}) = (I_z(\mathbf{x}) - \langle I_z(\mathbf{x}) \rangle_{ROI})^2$ if $\mathbf{x}$ belongs to the ROI and $V_z(\mathbf{x}) = 0$ otherwise. As it can be appreciated in Figure S7D panel b , $V_z(\mathbf{x})$ highlights localized intensity fluctuations with respect to mean value and captures heterogeneities in the spatial distribution of CytochromeC.

For each plane z, we calculated the coefficient of variation $CV(z)$ as the square root of the mean value of $V_z(\mathbf{x})$ over the ROI, normalized by the mean intensity $\langle I_z(\mathbf{x}) \rangle_{ROI}$

$$CV(z) = \frac{\sqrt{\langle V_z(\mathbf{x}) \rangle_{ROI}}}{\langle I_z(\mathbf{x}) \rangle_{ROI}}.$$

Once identified the plane z where $CV(z)$ has an absolute maximum, we used the corresponding value CV_0 as an indicator of the degree of spatial heterogeneity in the CytochromeC intensity distribution in the cell.

The described procedure, which for each cell focuses on the plane of maximum contrast in the CytochromeC intensity distribution, is aimed to avoid potential biases introduced by systematic differences in thickness and overall fluorescence intensity between differently treated cells.

All the described calculations have been implemented in a custom MATLAB code (CytochromeC_Quantification.m included in supplemental information).

Quantification of gH2AX foci

Mitotic cells were manually segmented using the DAPI signal. gH2AX foci were counted on the maximum projection using a custom Fiji scripts (gH2AX_Foci_Quantification.py included in supplemental information) created by Dr. Emanuele Martini (IFOM-ETS).

Statistical analysis

Statistical analysis and graph production was performed using R software. Statistical details, number of biological replicates (N), technical replicates and sample size (n) are reported in each figure legend.